Fast High-Fidelity Gates for Galvanically-Coupled Fluxonium Qubits Using Strong Flux Modulation

D.K. Weiss,[1,*] Helin Zhang,[2,3] Chunyang Ding,[2,3] Yuwei Ma,[2,3] David I. Schuster,[2,3,4] and Jens Koch[1]

[1] *Department of Physics and Astronomy, Northwestern University, Evanston, Illinois 60208, USA*
[2] *James Franck Institute, University of Chicago, Chicago, Illinois 60637, USA*
[3] *Department of Physics, University of Chicago, Chicago, Illinois 60637, USA*
[4] *Pritzker School of Molecular Engineering, University of Chicago, Chicago, Illinois 60637, USA*

(Received 14 July 2022; accepted 18 November 2022; published 27 December 2022)

Long coherence times, large anharmonicity, and robust charge-noise insensitivity render fluxonium qubits an interesting alternative to transmons. Recent experiments have demonstrated record coherence times for low-frequency fluxonium qubits. Here, we propose a galvanic coupling scheme with flux-tunable XX coupling. To implement a high-fidelity entangling $\sqrt{i\mathrm{SWAP}}$ gate, we modulate the strength of this coupling and devise variable-time identity gates to synchronize required single-qubit operations. Both types of gates are implemented using strong ac flux drives, lasting for only a few drive periods. We employ a theoretical framework capable of capturing qubit dynamics beyond the rotating-wave approximation as required for such strong drives. We predict an open-system fidelity of $F > 0.999$ for the $\sqrt{i\mathrm{SWAP}}$ gate under realistic conditions.

DOI: 10.1103/PRXQuantum.3.040336

I. INTRODUCTION

A major challenge in the field of quantum computing is to break free from the imperfections characteristic of the noisy intermediate-scale quantum (NISQ) era [1]. For superconducting qubits, this will specifically require further improvements of two-qubit gate performance beyond the current state of the art, with errors on the order of $10^{-3} - 10^{-4}$ [2–4]. To reach even lower two-qubit gate infidelities, it is worth reexamining the framework routinely used for developing the pulse trains that generate the gates of interest. Most commonly, this framework is intimately linked to the use of the rotating-wave approximation (RWA). This approximation is highly convenient as it can help remove fast time dependence from the Hamiltonian, yields an intuitive picture of the dynamics, and makes calculations particularly simple [5]. However, the range of validity of the RWA is limited and reliance on it constrains the parameter space that is explorable for maximizing gate fidelities. For low-frequency qubits such as heavy fluxonium [6–8], this is particularly unfortunate, as higher gate fidelities can indeed be achieved for parameter choices outside the reach of the RWA.

Here, we employ a theoretical framework based on the Magnus expansion [9–12], supplemented by full numerics, for executing high-fidelity gates in the regime of strong driving where drive amplitudes approach or even exceed the qubit frequency [8,13–15]. Motivated by the hundreds of microseconds [8,16] to millisecond [17] coherence times recently observed in low-frequency fluxonium qubits, we apply this analysis to a coupled system of such fluxonium qubits. For the case of capacitive coupling, previous work has focused on two-qubit gates effected via utilizing the microwave-activated cross-resonance effect [3], flux tuning energy levels into and out of resonance [18,19], and traversals through [20] or virtual excitations of [21] higher-lying states. These experimental realizations have been accompanied by a flurry of theoretical attention [22–28]. The fluxonium qubits considered in this context have frequencies on the order of 500 MHz to 1 GHz, generally thought to be the ideal frequency range for executing high-fidelity gates in these systems (considering gate schemes involving population transfer only in the qubit subspace) [22,23,25]. However, fluxonium qubits with frequencies less than 200 MHz have consistently achieved the longest coherence times [8,17], likely due to the scaling of the dielectric loss rate with the qubit frequency [8,16,17]. It is natural, in this case, to consider coupling the fluxonium qubits inductively [27,28], instead

*dkweiss@u.northwestern.edu

of capacitively [3,18–26]. To this end, we revisit inductive-coupling schemes previously proposed for and experimentally realized in flux qubits [29–33] and gmons [34,35].

We consider fluxonium qubits linked galvanically via a flux-tunable coupler. To avoid directly exciting the coupler degrees of freedom, the interaction between the qubits and the coupler is chosen to be dispersive. This allows for an effective description in which the coupler is eliminated but mediates a tunable XX interaction. We show that the strength of this effective XX coupling changes sign as a function of the coupler flux and thus passes through zero. In addition, we find that the parasitic ZZ interaction strength is suppressed, which is a general feature of coupled systems of low-frequency fluxonium qubits [20].

We describe how to execute two-qubit gates via parametric modulation of the coupler flux for a duration as short as a few drive periods. Based on our analysis outside the RWA regime, we find that the implemented entangling operations generally differ from named gates by relative phases. We compensate for these phase factors using single-qubit Z rotations to obtain a high-fidelity $\sqrt{i\mathrm{SWAP}}$ gate.

Ordinarily, single-qubit gates are designed in the convenient regime where RWA applies [5]. In this scenario, the switch into a frame corotating with the drive renders operations simple rotations about fixed axes in the Bloch-sphere picture. Identity gates are obtained by idling and single-qubit Z rotations are obtained either, e.g., "virtually," by modifying the phase of the drive field in software [36,37], or "physically," by detuning the qubit frequency from that of the drive [38]. The situation is reversed for systems of heavy-fluxonium qubits [6,7], where drive strengths exceeding the RWA range are employed—motivating the use of the laboratory frame for qubit operations [8,13]. In this frame, qubits acquire dynamical phases in the absence of control pulses; in other words, idling for a certain amount of time yields Z rotations of each qubit [8,13]. To synchronize gates in multiqubit systems, identity gates of variable time duration must be devised. We show that identity gates can again be implemented using sinusoidal modulation of the qubit fluxes for only a single drive period, resulting in ultrafast I gates (when compared to the single-qubit Larmor period). Combining the identity gates with single-qubit Z rotations assists in achieving high-fidelity entangling gates.

This paper is organized as follows. We introduce the coupling scheme in Sec. II and derive the full-circuit Hamiltonian and its effective counterpart governing the low-energy physics. We describe the implementation of single-qubit gates in Sec. III, focusing specifically on the needed identity gates. In Sec. IV, we detail our scheme for performing high-fidelity two-qubit gates, including the necessary single-qubit Z rotations and identity gates. In Sec. V, we summarize our results and provide an outlook on future work.

II. GALVANICALLY-COUPLED HEAVY-FLUXONIUM QUBITS

We consider galvanically linking two fluxonium qubits via a flux-tunable coupler. We bias the heavy-fluxonium qubits at their half-flux sweet spots, as such qubits are linearly insensitive to flux noise and thus have achieved record coherence times [8,16,17]. The qubit states are delocalized over two neighboring wells of the fluxonium potential, with the qubit frequency set by the tunnel splitting [39,40]. Single-qubit gates can be achieved by tuning the external flux away from the sweet spot, activating a transverse X interaction [8]. A galvanic coupling scheme helps yield strong coupling strengths, as those are quantified by phase matrix elements rather than charge matrix elements (as would be the case for capacitive coupling). Phase matrix elements are not suppressed by the qubit frequency [27], making a galvanic coupling architecture attractive for achieving entangling gates on low-frequency qubits. Moreover, for fluxonium qubits whose inductance is kinetic [40] rather than geometric [41], a galvanic connection can generally yield stronger coupling strengths than those achieved through mutual inductance alone [42–44]. To obtain a galvanic coupler with tunable coupling strength, we utilize a well-known architecture previously employed in experiments with flux qubits [32,33] and gmons [35] (see Fig. 1). These previous works have focused on coupling qubits with frequencies in the (1–7)-GHz range [32,33,35]. Here, we demonstrate that this coupler can

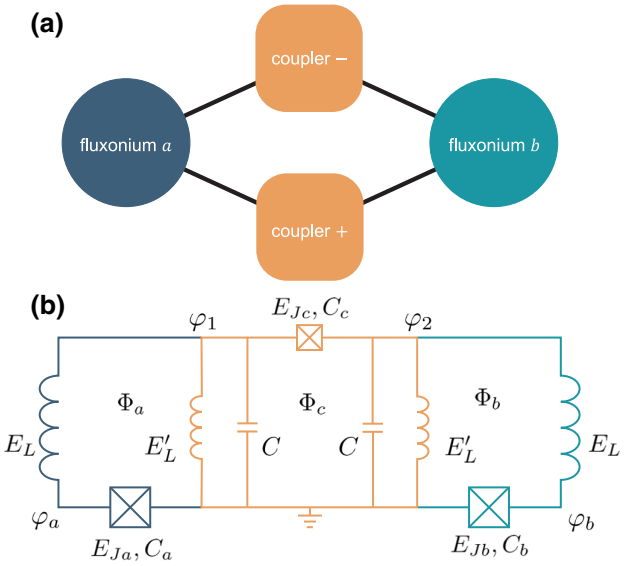

FIG. 1. Galvanically-coupled heavy-fluxonium qubits. (a) A schematic of the qubit-coupler interaction. The fluxonium qubits a and b are each coupled to a harmonic coupler mode θ_+ and a flux-tunable coupler mode θ_- but do not interact directly. (b) The circuit diagram of the device. Qubit a (dark blue) and qubit b (light blue) are galvanically linked to the two coupler modes $\theta_\pm$ (orange). Each loop can be threaded by an external flux Φ_μ.

also be used to obtain fast gates on low-frequency qubits. We slightly generalize the coupler by allowing for a stray capacitance C. This gives rise to a harmonic coupler mode, in addition to one that is fluxoniumlike and thus flux tunable. We show that the coupling strengths between the two qubits mediated by each of these modes enter with opposite signs and can be made to cancel by tuning the coupler flux. (We note that the coupler can also be understood as a generalization of the "fluxonium-molecule" circuit [45]). The circuit Hamiltonian is $H = H_0 + V$, where

$$\begin{aligned} H_0 = &\sum_{\mu=a,b} [4E_{C\mu} n_\mu^2 + \frac{1}{2} E_L \varphi_\mu^2 - E_{J\mu} \cos(\varphi_\mu + \pi)] \\ &+ 4E_{C-} n_-^2 + \frac{1}{2} E_{Lc} \theta_-^2 - E_{Jc} \cos(\theta_- + \phi_c) \\ &+ 4E_{C+} n_+^2 + \frac{1}{2} E_{Lc} \theta_+^2, \end{aligned} \tag{1}$$

$$\begin{aligned} V = &-\frac{E_L}{2} [\varphi_a(\theta_+ + \theta_-) + \varphi_b(\theta_+ - \theta_-)] \\ &+ \sum_{\mu=a,b} \frac{E_L}{2} \delta\phi_\mu [-2\varphi_\mu + \theta_+ + (-1)^\mu \theta_-], \end{aligned} \tag{2}$$

where μ obeys the correspondence $a \to 0, b \to 1$ when appearing in an exponent (for details on the full derivation of the Hamiltonian H, see Appendix A). We define the inductive energy of the coupler $E_{Lc} = \frac{1}{2}(E_L + E_L')$ and the charging energies $E_{C\mu} = e^2/2C_\mu$—in which $\mu = a, b$—$E_{C+} = e^2/(2[C/2])$, and $E_{C-} = e^2/(2[C_c + C/2])$, where the remaining circuit parameters can be read off from Fig. 1. The node variables φ_a, φ_b are the qubit variables, while the coupler variables are defined as $\theta_\pm = \varphi_1 \pm \varphi_2$. We isolate the qubit-flux shifts away from the sweet spot $\delta\phi_\mu = \phi_\mu - \pi$, where $\phi_\mu = 2\pi\Phi_\mu/\Phi_0$ is the reduced external flux, Φ_μ is the external flux in the corresponding loop, and $\Phi_0 = h/2e$ is the superconducting flux quantum.

The Hamiltonian H is composed of two fluxonium qubits and two coupler degrees of freedom, where the qubits interact with the coupler via terms in V. The coupler θ_+ degree of freedom is harmonic and has the mode frequency $\omega_+ = \sqrt{8E_{C+}E_{Lc}}$, while the coupler θ_- degree of freedom is fluxoniumlike and thus tunable by external flux. It is important to note that there is no term in the Hamiltonian directly coupling the qubits; thus the qubit-qubit interaction is entirely mediated by the coupler. Here, we assume symmetric qubit inductors, coupler inductors, and stray coupler capacitances, respectively (see Fig. 1). In this case, there are no terms in the Hamiltonian that directly couple the coupler degrees of freedom. This assumption is relaxed in Appendix A, where we derive the Hamiltonian in the presence of disorder in circuit parameters.

The coupler should have the following two desired properties. The first is that it must allow for the execution of high-fidelity two-qubit gates. A straightforward way to achieve this goal is to ensure that the interaction of the qubits with the coupler degrees of freedom is dispersive, allowing for an effective description in terms of two coupled qubits. The second requirement is that the two-qubit coupling strength should be sufficiently flux dependent, allowing for tuning from zero to values that allow for fast gates compared with the coherence times T_1, T_2 of each qubit. In the next section, we derive the effective Hamiltonian of the system assuming that the qubit-coupler interaction is dispersive. Following this, we discuss specific coupler-parameter choices that satisfy the above requirements.

A. Low-energy effective Hamiltonian

Near the half-flux sweet spots for each qubit, the qubit excitation energies are small compared with the energy needed to excite the coupler or higher-lying fluxonium states. These energy scales naturally define two subspaces: the low-energy subspace defined by the projector onto the computational states $P = \sum_{\ell,m=0,1} |\ell_a, m_b, 0_-, 0_+\rangle\langle \ell_a, m_b, 0_-, 0_+|$ and the high-energy subspace spanned by all other states. We define the bare states $|\ell_a, m_b, n_-, p_+\rangle$ that are eigenstates of H_0 with eigenenergies $E_l^a + E_m^b + E_n^- + p\omega_+$. The variables ℓ, m, n, p correspond to the number of excitations in the degrees of freedom corresponding to the variables φ_a, φ_b, θ_-, and θ_+, respectively. The coupler θ_- mode is fluxoniumlike; however, it is operated in a different parameter regime than the heavy-fluxonium qubits. The bare wave functions and spectra of qubit a and the coupler θ_- mode are shown in Fig. 2. We discuss below, in detail, the ideal parameter regime in which to operate the coupler modes.

States in different subspaces are coupled by the perturbation V, which is small compared with the relevant energy separations. Thus, the interaction is dispersive and we can obtain an effective description of the low-energy physics via a Schrieffer-Wolff transformation [5,46–48]. This is done by introducing a unitary e^{-S} with anti-Hermitian generator S that decouples the high- and low-energy subspaces order by order. We find the effective Hamiltonian up to second order upon projecting onto the low-energy subspace

$$H_{\text{eff}} = -\sum_{\mu=a,b} \frac{\omega_\mu'}{2} \sigma_z^\mu + J\sigma_x^a \sigma_x^b - \sum_{\mu=a,b} \Omega_\mu \sigma_x^\mu. \tag{3}$$

This transformation is carried out in detail in Appendix B. The Hamiltonian H_{eff} describes two qubits with frequencies $\omega_\mu' = \omega_\mu + \chi_\mu$, where $\omega_\mu = E_1^\mu - E_0^\mu$ are the bare qubit frequencies (here and in the following, we set $\hbar = 1$) and χ_μ are the Lamb shifts. The qubits are coupled via a transverse XX interaction with strength J that is tunable with coupler flux ϕ_c. There are additional single-qubit X

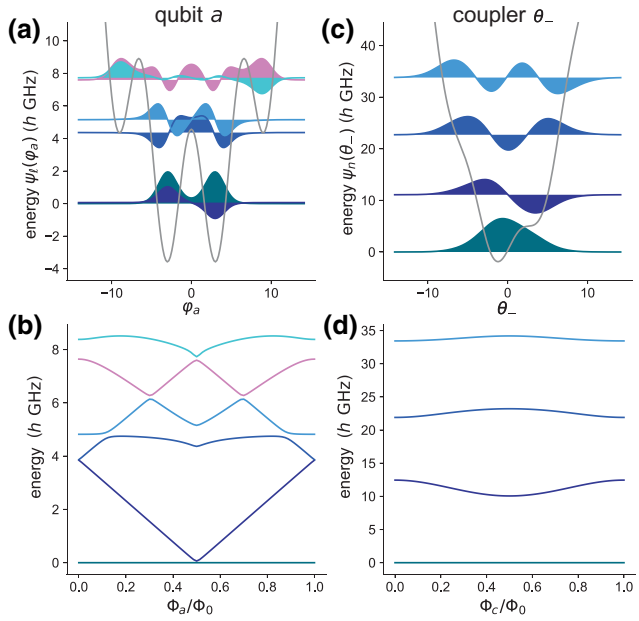

FIG. 2. Bare wave functions and energy spectra. (a) The bare wave functions and potential of qubit a, located at the half-flux sweet spot. The bare-qubit transition frequency is $\omega_a/2\pi = 62$ MHz, while the energy of the next excited state is 4.3 h GHz above the energy of the first-excited state. (b) The spectrum of qubit a as a function of the qubit flux Φ_a. The wave functions and spectra of qubit b are qualitatively similar to those of qubit a. (c) The bare wave functions and potential of the coupler θ_- mode, located at $\Phi_c/\Phi_0 = 0.27$. The energy of the first excited state is more than 10 h GHz above the coupler ground-state energy. (d) The spectrum of the coupler θ_- mode as a function of the coupler flux ϕ_c. See Table I for device parameters as well as Table II for a summary of the frequencies and anharmonicities of the bare modes.

terms with strength Ω_μ that depend on the coupler flux ϕ_c as well as the qubit fluxes $\delta\phi_\mu$. We show below that both J and Ω_μ can be tuned through zero, yielding two decoupled qubits. The coefficient Ω_μ is defined as

$$\Omega_\mu = E_L \langle 0_\mu|\varphi_\mu|1_\mu\rangle \left[\delta\phi_\mu + (-1)^\mu \frac{\langle 0_-|\theta_-|0_-\rangle}{2}\right] \quad (4)$$

and arises at first order in perturbation theory from two contributions. The first term on the right-hand side is due to a qubit-flux offset from the sweet spot $\delta\phi_\mu$, while the second is from the coupling between the qubits and the coupler θ_- mode. The matrix element $\langle 0_-|\theta_-|0_-\rangle$ is ϕ_c dependent and generally nonzero due to the absence of selection rules for a fluxonium biased away from a sweet spot [49,50]. Interpreting this second term as an effective flux shift away from the sweet spot for each qubit, we cancel this shift by setting

$$\delta\phi_\mu = (-1)^{\mu+1} \frac{\langle 0_-|\theta_-|0_-\rangle}{2}. \quad (5)$$

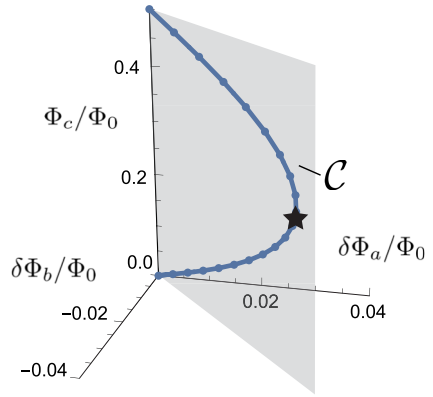

FIG. 3. The sweet-spot contour. As the coupler flux is tuned, the qubit fluxes must be simultaneously adjusted according to $\delta\Phi_\mu/\Phi_0 = (-1)^{\mu+1}\langle 0_-|\theta_-|0_-\rangle/4\pi$ in order to keep the qubits at their sweet spots $\Omega_\mu = 0$. The qubit fluxes are measured as deviations away from the bare sweet-spot locations. The sweet-spot contour $\mathcal{C}$ lies in the semitransparent gray plane, which bisects the angle between the two qubit-flux axes. The off position where $\Omega_\mu = J = 0$ is marked by a black star.

Thus, we obtain the coupler-flux-dependent "sweet-spot contour" shown in Fig. 3. It is important to note that this phenomenon is independent of effects due to geometric flux crosstalk and arises instead directly from coupling terms in V.

The two-qubit interaction arises at second order in perturbation theory, with strength $J = J_- - J_+$. The coefficient J_- (J_+) is due to interaction of the qubit with the coupler θ_- (θ_+) mode. The strength of the interaction J_- is tunable due to the dependence of the matrix elements $\langle 0_-|\theta_-|n_-\rangle$ and energies E_n^- on the coupler flux (for details, see Appendix B). The coefficient J_+ is static; thus the two-qubit interaction is eliminated by tuning J_- to equal J_+ in magnitude [51]. We can understand the XX nature of the two-qubit coupling by considering the terms appearing in V that mediate the interaction between different subsystems. At the qubit sweet spots and considering only the computational states, the operators φ_μ are off diagonal and therefore proportional to σ_x^μ with a proper choice of phases. Thus, the effective two-qubit interaction consists of a virtual second-order process whereby an excitation is exchanged between the two qubits, or both qubits are coexcited or codeexcited.

In what follows, we always operate from the dc-flux bias point on the sweet-spot contour $\Omega_\mu = 0$ where the two-qubit coupling is turned off $J = 0$ (see Fig. 3). We do this to keep both qubits at their respective sweet spots and to prevent any unwanted parasitic entanglement between the qubits. We refer to this configuration of dc fluxes as the "off position." Both single- and two-qubit gates are performed by ac flux excursions about this point. Note that the value of the coupler flux ϕ_c at the off position is generally

parameter dependent and not at a sweet spot. It is important to ensure, then, that the coupler θ_- mode is not overly flux sensitive to avoid indirectly causing the qubits to drift away from their respective sweet spots [see Eq. (4)].

B. Parameter regime of the coupler

To obtain an effective description in terms of two-coupled qubits, the parameter choices for the coupler should support a dispersive interaction. Additionally, we require that the coupling strength be sufficiently flux dependent, allowing both for the execution of fast gates and for the interaction to be efficiently turned off. We quantify the dispersiveness of the interaction by calculating the Lamb shift χ_a (we obtain similar results in the following utilizing χ_b instead). Considering the requirements on flux dependence, we calculate the slope of the coupling strength J_- with respect to Φ_c at the off position. We target parameters such that $|\partial_{\Phi_c} J_-|/h \approx 100\ \mathrm{MHz}/\Phi_0$ to achieve megahertz-level coupling strengths (implying fast gates compared with T_1, T_2) for small ac flux excursions $\Phi_c \lesssim 0.03\Phi_0$, where a linear relationship between the coupling strength J and flux Φ_c is expected to be valid. This value of the slope also ensures that the device remains insensitive to typical $1/f$ flux-noise amplitudes $A_\Phi \approx 1\mu\Phi_0$ [52].

We sweep over E_{Jc} and E_{C-} and calculate $|\partial_{\Phi_c} J_-|$ as well as χ_a at the off position (see Fig. 4). We fix $E_L'/h = 2$ GHz ($E_{Lc}/h = 1.1$ GHz); however, we obtain similar results when considering instead larger or smaller values of E_L'. It is worth emphasizing that the off position is parameter dependent; thus we reposition the dc fluxes appropriately for each parameter set. For relatively large E_{Jc} and small E_{C-}, the lowest-lying states at intermediate flux values localize in minima of the cosine potential. The off position is then generally near the sweet spot, where the vanishing energy difference between the states $|0_-\rangle, |1_-\rangle$, as well as the rapid increase in the value of the matrix element $|\langle 0_-|\theta_-|1_-\rangle|$, enable flux tunability of J_-. These factors in turn imply extreme sensitivity to flux $|\partial_{\Phi_c} J_-|/h \gg 100\ \mathrm{MHz}/\Phi_0$ as well as a breakdown of the dispersive regime. For relatively small E_{Jc} and large E_{C-}, flux tunability is lost, as the spectrum is nearly harmonic. For decreasing E_{Jc} and E_{C-}, the excitation energies are suppressed, leading to a breakdown of the dispersive interaction. The parameter regime that supports both a dispersive interaction and "Goldilocks" flux dependence is thus $E_{C-} > E_{Jc} \gtrsim E_{Lc}$. The parameters E_{C+} and E_{Lc} that define the coupler θ_+ mode are implied by the parameter choices for the coupler θ_- mode. This is due to the restriction $E_{C+} > E_{C-}$, noting that there is a finite junction capacitance. It is worth noting that the precise value of E_{C+} is largely uncontrollable as C is a stray capacitance. However, fine tuning of C is not necessary for the coupler to function as intended: we expect E_{C-} to be dominated by the junction capacitance C_c, set by the geometry of the coupler Josephson junction. Moreover, the coupling strength J is insensitive to E_{C+} in the parameter regime of interest (for details, see Appendix B). The parameters used in the remainder of this work are given in Table I and the resulting frequencies and anharmonicities of the various modes are detailed in Table II.

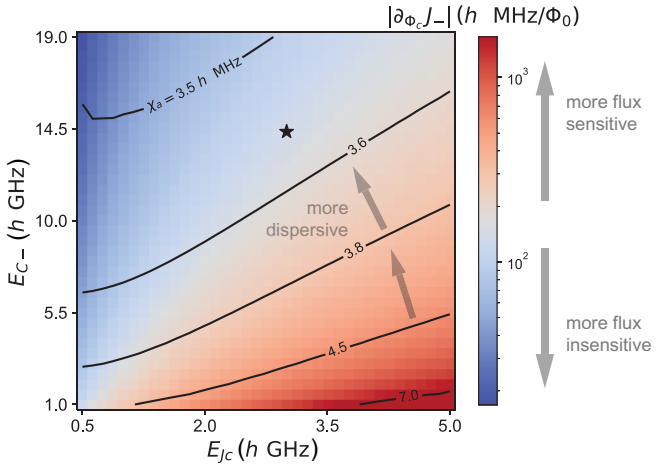

FIG. 4. The flux sensitivity and dispersiveness as a function of the coupler parameters E_{Jc} and E_{C-}. The coloring indicates $|\partial_{\Phi_c} J_-|$, i.e., the linear sensitivity of the coupling strength with respect to the flux. The contour lines quantify the dispersiveness of the qubit-coupler interaction via the Lamb shift χ_a. A dispersive interaction and suitable flux sensitivity are achieved in the parameter regime $E_{C-} > E_{Jc} \gtrsim E_{Lc}$. The star marks the chosen parameters (see Table I).

C. Numerical results

We compute the low-energy spectra of the full-model Hamiltonian H as well as the effective Hamiltonian H_{eff} and plot the results in Fig. 5(a). We vary the coupler flux along the contour $\mathcal{C}$ shown in Fig. 3 to ensure that the qubits remain at their sweet spots. The relative deviations between the two spectra are at the level of a percent or less, indicating that the exact results can be accurately described by an effective model of two qubits coupled by a tunable XX interaction. The value of the tunable-coupling coefficient J is shown in Fig. 5(b) and crosses through zero at $\phi_c \approx 0.27 \times 2\pi$. At this position in flux space, the coupler is in the "*off* " state.

TABLE I. The circuit parameters in h GHz used throughout this work.

E_{Ja}	E_{Jb}	E_{Ca}	E_{Cb}	E_L	E_{Jc}	E_L'	E_{C-}	E_{C+}
4.6	5.5	0.9	0.9	0.21	3	2	14.3	100

TABLE II. The energy splittings and anharmonicities of the bare modes. The fluxonium qubits are biased at their half-flux sweet spots, while the coupler θ_- mode is biased at $\Phi_c/\Phi_0 = 0.27$. The energy splittings are differences between the bare ground and first-excited-state energies $E_{10} = E_1 - E_0$, while the anharmonicity is defined as $\alpha = E_{21} - E_{10}$. All quantities are in units of h GHz.

	Qubit a	Qubit b	Coupler θ_-	Coupler θ_+
E_{10}	0.062	0.037	11	30
α	4.3	4.9	0.53	0

To quantify the *on-off* ratio of the tunable coupler, we numerically calculate the strength of the parasitic ZZ interaction using the formula $\zeta_{ZZ} = E_{\overline{1100}} - E_{\overline{1000}} - E_{\overline{0100}} + E_{\overline{0000}}$ [20]. The eigenenergy $E_{\overline{ijnp}}$ of the dressed state $|\overline{i_a, j_b, n_-, p_+}\rangle$ is found by numerically diagonalizing the full-model Hamiltonian H. The ZZ interaction strength ζ_{ZZ} is less than 0.3 h kHz at the *off* position for the parameters considered here, implying an *on-off* ratio of the order of 10^5. It is a general feature of coupled systems of low-frequency fluxonium qubits that ZZ interaction strengths are suppressed, due to the small repulsions between computational and noncomputational states [20].

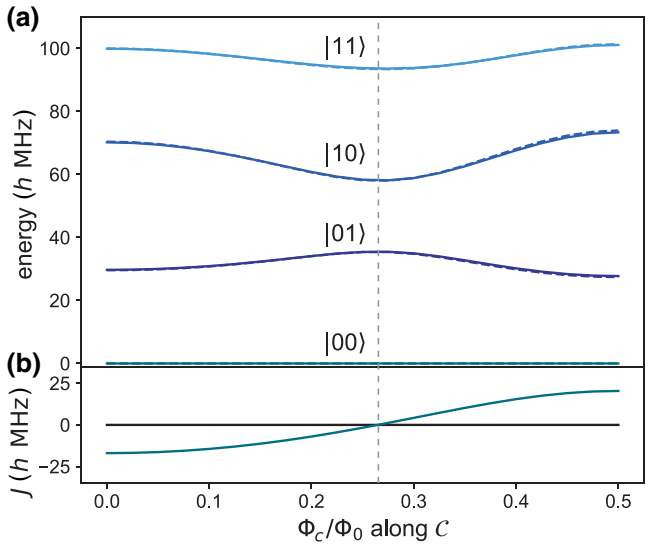

FIG. 5. (a) The low-energy spectrum of the coupled system. As the coupler flux is tuned, the qubit fluxes are adjusted to remain on the sweet-spot contour $\mathcal{C}$, ensuring that $\Omega_\mu = 0$. The full lines correspond to the exact spectrum calculated from the full-model H, while the dashed lines correspond to the spectrum as calculated from the effective Hamiltonian H_{eff}. The eigenenergies are labeled according to the bare state $|ij\rangle \equiv |i_a, j_b, 0_-, 0_+\rangle$, with the largest overlap with the corresponding dressed state when the coupler is in the off state (at $\phi_c \approx 0.27 \times 2\pi$, marked by the gray dashed line). (b) The strength J of the effective XX coupling. The device parameters can be found in Table I.

III. SINGLE-QUBIT GATES

There are important differences between how single-qubit gates are performed on high-frequency qubits such as transmons and how they are executed on low-frequency qubits such as those studied here. For transmon qubits, drive strengths are typically small compared with the qubit frequency. It is then appropriate to move into a frame corotating with the drive frequency (typically on or near resonance with the qubit frequency) and perform the RWA [5,53]. The rotating-frame Hamiltonian is now time independent, allowing for the relatively straightforward calculation of time-evolution operators (propagators). Observe that in this rotating frame, idling corresponds to an identity operation (assuming a resonant drive). In contrast, to obtain fast gates for low-frequency qubits such as heavy fluxonium [8] or superconducting composite qubits [13], drive strengths typically equal or exceed the qubit frequencies. Thus, gates are typically performed in the laboratory frame, as it is not appropriate to move into a rotating frame like that described above [8,13–15]. In the laboratory frame, qubit states acquire dynamical phase factors while idling. Indeed, we utilize these Z rotations in Sec. IV for achieving a high-fidelity $\sqrt{i\text{SWAP}}$ gate. Nevertheless, in the absence of drives, we obtain an identity operation (up to an overall sign) only by idling for exact multiples of the Larmor period $\tau_q = 2\pi/\omega_q$, where ω_q is the qubit frequency. If we now consider multiple qubits with noncommensurate frequencies, it is not obvious how to perform an operation on one qubit without a second qubit acquiring dynamical phase during the gate time. Therefore, we seek an active means of obtaining *variable-time* identity operations for low-frequency qubits. Single-qubit $X/2$ and $Y/2$ gates can be obtained using the techniques described in, e.g., Refs. [8,13], allowing for universal control when combined with arbitrary Z rotations achieved by idling.

We utilize flux pulses [54] that begin and end at zero and whose shapes are described by sinusoidal functions but that only last for a single period [13]. This pulse shape is chosen because the external flux averages to zero [55], helping to eliminate long-time-scale distortions [56]. The Hamiltonian of a single fluxonium biased at the half-flux sweet spot and subject to a sinusoidal flux drive $\phi(t) = \delta\phi \sin(\omega_d t)$ is $H_{\text{fl}}(t) = H_\pi + H_d(t)$, where

$$H_\pi = 4E_C n^2 - E_J \cos(\varphi) + \frac{1}{2}E_L(\varphi + \pi)^2, \quad (6)$$

$$H_d(t) = E_L \varphi \delta\phi \sin(\omega_d t). \quad (7)$$

Projecting onto the computational subspace yields [8]

$$H_q(t) = -\frac{\omega_q}{2}\sigma_z + A \sin(\omega_d t)\sigma_x, \quad (8)$$

defining the effective drive amplitude $A = E_L\langle 0|\varphi|1\rangle\delta\phi$ and making use of selection rules at the half-flux sweet

spot. For typical heavy-fluxonium parameters such as those chosen for qubits a and b, the amplitude of the drive A exceeds the qubit frequency ω_q for deviations from the sweet spot as small as $\delta\phi = 0.02 \times 2\pi$. Indeed, such strong drives have been used to implement fast single-qubit gates with high fidelities [8,13]. Here, we utilize similarly strong drives for the implementation of identity pulses. We seek conditions on the drive strength A and frequency ω_d such that the propagator $U_q(t)$ is equal to the identity operation after a single drive period, $U_q(t = 2\pi/\omega_d) = \mathbb{1}$. The propagator satisfies the time-dependent Schrödinger equation

$$\frac{dU_q(t)}{dt} = -iH_q U_q(t), \tag{9}$$

with the initial condition $U_q(0) = \mathbb{1}$. In the regime where the qubit frequency ω_q is small compared to the drive amplitude A, it is appropriate to move into the interaction picture defined with respect to the drive. This transformation is achieved via the unitary

$$\begin{aligned} U_0(t) &= \exp\left(-i\int_0^t dt'\, A\sin[\omega_d t]\sigma_x\right) \\ &= \exp\left(-i\frac{2A}{\omega_d}\sin^2\left[\frac{\omega_d t}{2}\right]\sigma_x\right). \end{aligned} \tag{10}$$

The interaction-frame Hamiltonian is

$$\begin{aligned} H_q' &= U_0^\dagger H_q U_0 - iU_0^\dagger \dot{U}_0 \\ &= -\frac{\omega_q}{2}\cos\left(\frac{4A}{\omega_d}\sin^2\left[\frac{\omega_d t}{2}\right]\right)\sigma_z \\ &\quad -\frac{\omega_q}{2}\sin\left(\frac{4A}{\omega_d}\sin^2\left[\frac{\omega_d t}{2}\right]\right)\sigma_y, \end{aligned} \tag{11}$$

while the propagator in this frame $U_q'(t)$ satisfies $dU_q'(t)/dt = -iH_q'U_q'(t)$. To obtain an approximation to the propagator $U_q'(t)$, we carry out a Magnus expansion [9–11] in which the propagator is assumed to take an exponential form $U_q'(t) = \exp(\sum_{i=1}^{\infty}\Delta_i(t))$. The first term in this series is $\Delta_1(t) = -i\int_0^t H_q'(t')dt'$ and the formulas for terms up to fourth order are given in, e.g., Refs. [10,11]. We truncate the Magnus series after the first term, as we find that higher-order terms are generally small and can be neglected. The propagator at the conclusion of the pulse is

$$\begin{aligned} U_q'(\tau_d) &= \cos\left(\frac{\pi\omega_q}{\omega_d}J_0\left[\frac{2A}{\omega_d}\right]\right)\mathbb{1} + i\sin\left(\frac{\pi\omega_q}{\omega_d}J_0\left[\frac{2A}{\omega_d}\right]\right) \\ &\quad\times\left(\cos\left[\frac{2A}{\omega_d}\right]\sigma_z + \sin\left[\frac{2A}{\omega_d}\right]\sigma_y\right), \end{aligned} \tag{12}$$

where $\tau_d = 2\pi/\omega_d$ and J_0 is the zeroth-order Bessel function of the first kind. The propagators in the laboratory and interaction frames are related by $U_q(t) = U_0(t)U_q'(t)U_0^\dagger(0)$. Because the laboratory and interaction frames coincide at $t = 0$ and $t = \tau_d$, the propagators in the laboratory and interaction frames are the same at the conclusion of the pulse. To obtain an identity gate, the general solution is

$$\frac{\pi\omega_q}{\omega_d}J_0\left(\frac{2A}{\omega_d}\right) = 2\pi r, \quad r \in \mathbb{Z}, \tag{13}$$

which is an equation for the variables A and ω_d. Solutions that avoid fixing ω_d based on the value of ω_q are those for $r = 0$ that satisfy

$$\frac{2A}{\omega_d} = j_k, \quad k = 1, 2, \ldots, \tag{14}$$

where j_k is the kth zero of J_0. Thus, by choosing a combination of drive amplitude A and frequency ω_d (and thus gate time) obeying Eq. (14), we obtain a variable-time identity gate. We note that it is also possible to arrive at Eq. (13) using a perturbative analysis in the context of Floquet theory [57].

We present numerical results illustrating that the proposed identity gates can be achieved with high fidelity. To calculate the closed-system fidelity of a quantum operation, we utilize the formula [58]

$$F = \frac{\mathrm{Tr}(U^\dagger U) + |\,\mathrm{Tr}[U_T^\dagger U]|^2}{d(d+1)}, \tag{15}$$

where d is the dimension of the relevant subspace of the Hilbert space, U_T is the target unitary, and U is the projection onto the d-dimensional subspace of the propagator realized by time evolution. This formula is especially useful when considering systems where leakage may be an issue; in such cases, deviations of the operator U from unitarity are penalized by the term $\mathrm{Tr}(U^\dagger U)$. To obtain the propagator associated with time evolution under the Hamiltonian $H_{\mathrm{fl}}(t)$, it is most appropriate to express $H_{\mathrm{fl}}(t)$ in the eigenbasis of the static Hamiltonian H_π. The qubit states are the two lowest-energy states and we retain up to eight eigenstates to monitor leakage. Diagonalization of H_π is done using the SCQUBITS software package [59], while time-dependent simulations are performed using the QuTiP software package [60,61]. Sweeping over the drive frequency and amplitude of the flux pulse, we monitor the fidelity of an identity operation, taking $d = 2$ and $U_T = \mathbb{1}$ in Eq. (15) (see Fig. 6).

Regions of high fidelity appear as "fingers" in the space of inverse gate time (drive frequency ω_d) and effective drive amplitude A. The colored lines are given by $A = j_k\omega_d/2$ for $k = 1, 2, 3, 4, 5$, corresponding to the drive parameters that analytically predict identity gates. These lines overlap with the regions of high fidelity computed numerically for large-amplitude A compared with the qubit

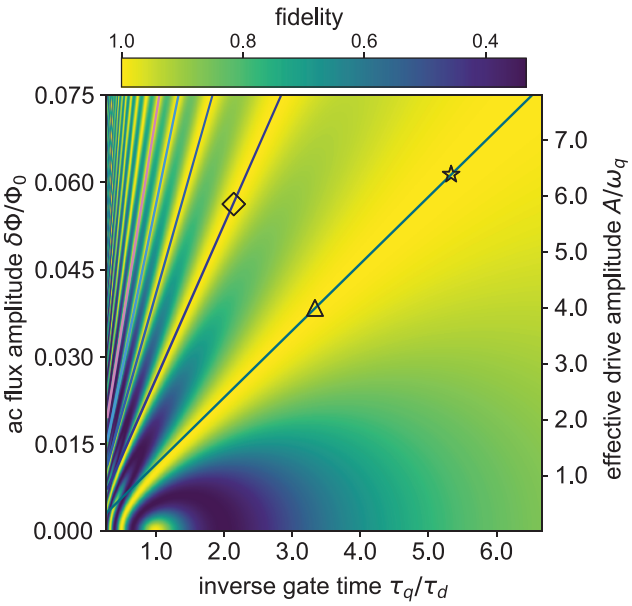

FIG. 6. A variable-time single-qubit identity pulse. We plot the fidelity of an identity operation under a single-period sinusoidal qubit-flux drive. The lines mark locations in amplitude and frequency space where $A = j_k\omega_d/2$ for the first five zeroes j_k of J_0. Multiple other lines of high fidelity corresponding to larger zeros of J_0 are visible in the numerics. These variable-time identity gates are ultrafast, with gate times that can be small compared to the Larmor period. The pointlike region of high fidelity at $\delta\phi = 0$ corresponds to the passive identity operation. The marked points label example drive parameters used for visualizing Bloch-sphere trajectories in Fig. 7. The numerical simulations are performed using the parameters of qubit b, where $\omega_q/2\pi = 37$ MHz.

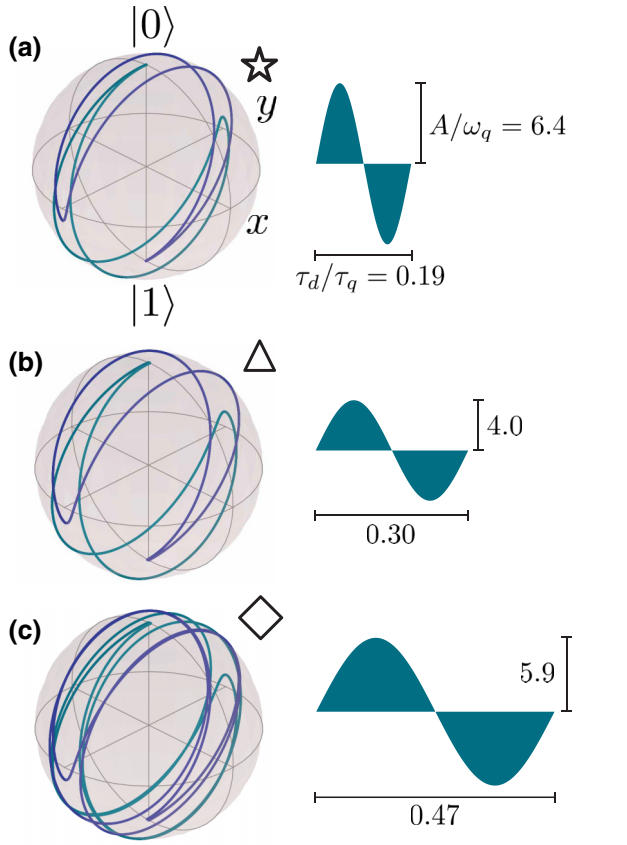

FIG. 7. (a)-(c) The Bloch-sphere trajectory in the laboratory frame of the initial states $|0\rangle$ and $|1\rangle$ subject to the pictured identity gates. The pulse parameters utilized here are marked in Fig. 6. Each gate achieves an identity operation with fidelity $F \geq 0.9998$.

frequency ω_q. For decreasing ω_d and A, the lines begin to deviate from the high-fidelity fingers due to the breakdown of the Magnus expansion [10]. Nevertheless, we find numerically that high-fidelity $F > 0.9999$ identity gates can be achieved across a wide range of inverse gate times $0.5 \lesssim \omega_d/\omega_q \lesssim 7$. Leakage outside the computational subspace is negligible for the parameters considered here.

The time evolution of the qubit states in the laboratory frame in the form of trajectories on the Bloch sphere during identity pulses is shown in Fig. 7. The drive frequencies ω_d used in Figs. 7(a)–7(c) are $\omega_d/\omega_q = 5.3$, 3.3, and 2.1, with drive amplitudes A obtained from Eq. (14) using the Bessel zeros j_1, j_1, and j_2, respectively. In all three cases, we obtain fidelities of $F \geq 0.9998$. Numerical optimization of the drive amplitude keeping the drive frequency fixed yields $F > 0.999\,99$ in each case. The optimized amplitude generally differs from the amplitude derived analytically by less than or of the order of a percent.

In this section, we have analyzed an isolated heavy fluxonium subject to an ac flux drive. The generalization to fluxonium qubits embedded in the architecture considered in this work is straightforward. At the off position, the operator activated by a flux drive on qubit a and b is to a good approximation of the form of XI and IX, respectively (for details, see Appendix C). Thus, the identity-gate protocol is immediately applicable to each individual qubit.

IV. TWO-QUBIT ENTANGLING GATE

When performing two-qubit gates on low-frequency fluxonium qubits, we encounter similar issues to those present for single-qubit gates. To achieve relatively fast gate times compared with T_1 and T_2, we utilize drive strengths where the RWA is invalid. We perform a Magnus expansion in a frame corotating with the qubit frequencies to account for the counter-rotating terms order by order. We note that similar results can be obtained using a Floquet analysis [62,63]. Because single-qubit gates are performed in the laboratory frame, we then transform the rotating-frame propagator back into the laboratory frame.

To activate a two-qubit interaction, we consider an ac sinusoidal coupler flux drive $\phi_c(t) = \delta\phi_c \sin(\omega_d t)$. The time-dependent Hamiltonian in the computational subspace is

$$H_{2q}(t) = -\frac{\omega_a'}{2}\bar{\sigma}_z^a - \frac{\omega_b'}{2}\bar{\sigma}_z^b + A\sin(\omega_d t)\bar{\sigma}_x^a\bar{\sigma}_x^b, \quad (16)$$

where we emphasize that gates are performed in the basis of the dressed states (for details, see Appendix C). The Pauli matrices are defined as, e.g., $\bar{\sigma}_x^a = \sum_{j=0,1} |\overline{0j}\rangle\langle\overline{1j}| +$ H.c., etc., utilizing the shorthand $|\overline{i_a j_b}\rangle \equiv |\overline{i_a, j_b, 0_-, 0_+}\rangle$. The effective drive amplitude $A \equiv J_{\rm ac}\delta\phi_c$ is defined in terms of the ac two-qubit coupling strength $J_{\rm ac}$ given in Eq. (C15). For our parameters, $J_{\rm ac}/h = 18.3$ MHz. Just as for single-qubit gates, we drive with $\sin\omega_d t$ rather than $\cos\omega_d t$ because we intend to activate the interaction for only one or a few drive periods n [64]. In general, the propagator at the final time $\tau_n = 2\pi n/\omega_d$ is

$$U(\tau_n) = \mathcal{T}e^{-i\int_0^{\tau_n} H_{2q}(t')dt'} = \begin{pmatrix} a & 0 & 0 & d \\ 0 & b & c & 0 \\ 0 & -c^* & b^* & 0 \\ -d^* & 0 & 0 & a^* \end{pmatrix}, \quad (17)$$

where $\mathcal{T}$ is the time-ordering operator and $|a|^2 + |d|^2 = |b|^2 + |c|^2 = 1$. To obtain an entangling gate, we target drive parameters A, ω_d that yield $|b| = |c| = 1/\sqrt{2}$ and $d = 0$ [65]. We parametrize this gate as

$$\sqrt{\phi\text{SWAP}} = \begin{pmatrix} e^{i\alpha} & 0 & 0 & 0 \\ 0 & e^{i\beta}/\sqrt{2} & e^{i\gamma}/\sqrt{2} & 0 \\ 0 & -e^{-i\gamma}/\sqrt{2} & e^{-i\beta}/\sqrt{2} & 0 \\ 0 & 0 & 0 & e^{-i\alpha} \end{pmatrix}. \quad (18)$$

To see that this gate is entangling, note that it can either produce Bell states or be transformed into the entangling gate

$$\sqrt{i\text{SWAP}} = \begin{pmatrix} 1 & 0 & 0 & 0 \\ 0 & 1/\sqrt{2} & -i/\sqrt{2} & 0 \\ 0 & -i/\sqrt{2} & 1/\sqrt{2} & 0 \\ 0 & 0 & 0 & 1 \end{pmatrix}, \quad (19)$$

using only single-qubit operations [66]. One such transformation using single-qubit gates is

$$\sqrt{i\text{SWAP}} = R_Z^a(\theta_{a1})R_Z^b(\theta_{b1})\sqrt{\phi\text{SWAP}}R_Z^a(\theta_{a2})R_Z^b(\theta_{b2}), \quad (20)$$

where

$$R_Z^j(\theta) = \exp(-i\theta\bar{\sigma}_z^j/2), \quad j = a, b.$$

Expressions for the Z rotation angles in Eq. (20) in terms of α, β, and γ are specified below. The relationship given in Eq. (20) provides an explicit recipe for constructing a $\sqrt{i\text{SWAP}}$ gate, given a $\sqrt{\phi\text{SWAP}}$ gate and arbitrary single-qubit Z rotations. Quantum algorithms are typically written in terms of named gates such as $\sqrt{i\text{SWAP}}$ [67–69], as opposed to the native gate $\sqrt{\phi\text{SWAP}}$ achieved here. Thus, it may be useful to immediately transform the obtained $\sqrt{\phi\text{SWAP}}$ gate into the more familiar $\sqrt{i\text{SWAP}}$. This is the strategy we pursue here.

Generally, only three of the Z rotations in Eq. (20) are necessary. We make use of the freedom of the extra Z rotation by choosing the angle $\theta_{b2} \in [0, 2\pi)$ that optimizes the overall gate time, including the Z rotations. The remaining angles are set to

$$\begin{aligned} \theta_{a1} &= \frac{\pi}{2} + \alpha + \gamma - \theta_{b2}, \\ \theta_{b1} &= \alpha - \beta - \theta_{b2}, \\ \theta_{a2} &= -\frac{\pi}{2} + \beta - \gamma + \theta_{b2}, \end{aligned} \quad (21)$$

to satisfy Eq. (20). In the following, we find explicit expressions for α, β, and γ in terms of the drive parameters and qubit frequencies. Because we operate in the laboratory frame, these Z rotations are obtained by idling. Idle times for coincident Z rotations may differ in general; therefore, to synchronize the time spent performing single-qubit gates, we make use of the variable-time single-qubit identity gates discussed in Sec. III.

A. Constructing $\sqrt{\phi\text{SWAP}}$

The propagator $\sqrt{\phi\text{SWAP}}$ can be obtained from time evolution under the Hamiltonian $H_{2q}(t)$ as follows. The qubit frequencies ω_a', ω_b' are fixed by operating the qubits at their sweet spots, while the drive parameters A, ω_d may be varied. The Hamiltonian $H_{2q}(t)$ only couples the pairs of states $|\overline{00}\rangle \leftrightarrow |\overline{11}\rangle$ and $|\overline{01}\rangle \leftrightarrow |\overline{10}\rangle$; thus $H_{2q}(t)$ decomposes into a direct sum $H_{2q}(t) = H_-(t) \bigoplus H_+(t)$, where

$$H_\pm(t) = -\frac{\omega_\pm}{2}\Sigma_z^\pm + A\sin(\omega_d t)\Sigma_x^\pm, \quad (22)$$

defining $\omega_\pm = \omega_a' \pm \omega_b'$. The Hamiltonians $H_+(t)$ and $H_-(t)$ describe dynamics in the $|\overline{00}\rangle, |\overline{11}\rangle$, and $|\overline{01}\rangle, |\overline{10}\rangle$ subspaces, respectively. The corresponding Pauli matrices are denoted by $\Sigma_j^\pm$, e.g., $\Sigma_z^+ = |\overline{00}\rangle\langle\overline{00}| - |\overline{11}\rangle\langle\overline{11}|$. For realistic parameters, the two-level-system frequencies ω_+ and ω_- are large compared with the drive amplitude A. In this case, it is appropriate to move into the interaction

picture defined by the unitaries

$$U_0^{\pm}(t) = \exp\left[i\frac{\omega_{\pm}}{2}\Sigma_z^{\pm}t\right]. \tag{23}$$

The interaction-frame Hamiltonians are

$$H'_{\pm}(t) = A\sin(\omega_d t)[\cos(\omega_{\pm}t)\Sigma_x^{\pm} + \sin(\omega_{\pm}t)\Sigma_y^{\pm}]. \tag{24}$$

To calculate the associated propagators, we carry out a Magnus expansion including the first- and second-order terms. It is straightforward to calculate higher-order corrections; however, we find for our parameters that they are small and can be neglected. The expression for the propagator is then $U'_{\pm}(t) = \exp(\Delta_1^{\pm}[t] + \Delta_2^{\pm}[t])$, where [9–11]

$$\Delta_1^{\pm}(t) = -i\int_0^t H'_{\pm}(t')dt', \tag{25}$$

$$\Delta_2^{\pm}(t) = -\frac{1}{2}\int_0^t dt_1\int_0^{t_1} dt_2[H'_{\pm}(t_1), H'_{\pm}(t_2)]. \tag{26}$$

At the conclusion of the gate $t = \tau_n$, we obtain

$$U'_{\pm}(\tau_n) = \cos(\xi_{\pm})\,\mathbb{1} - i\sin(\xi_{\pm})\,(\vec{n}_{\pm}\cdot\vec{\Sigma}^{\pm}), \tag{27}$$

where

$$\vec{n}_{\pm} = (\sin[\pi n\omega_{\pm}/\omega_d], -\cos[\pi n\omega_{\pm}/\omega_d], \varepsilon_{\pm}/\xi_{\pm}), \tag{28}$$

$$\vec{\Sigma}^{\pm} = \left(\Sigma_x^{\pm}, \Sigma_y^{\pm}, \Sigma_z^{\pm}\right), \tag{29}$$

and we define

$$\xi_{\pm} = \frac{2A\omega_d}{\omega_d^2 - \omega_{\pm}^2}\sin\left(\frac{\pi n\omega_{\pm}}{\omega_d}\right),$$

$$\varepsilon_{\pm} = \frac{A^2\omega_d^2\sin(2\pi n\omega_{\pm}/\omega_d)}{(\omega_d^2-\omega_{\pm}^2)^2} + \frac{A^2\pi n\omega_{\pm}}{\omega_d(\omega_d^2-\omega_{\pm}^2)}. \tag{30}$$

We neglect corrections of order $\mathcal{O}([A/\omega_d]^3)$ to $\xi_{\pm}$. The first-order terms involving $\Sigma_x^{\pm}$, $\Sigma_y^{\pm}$ determine the amount of population transfer between the two states in each subspace. The second-order terms encode the leading-order beyond-the-RWA corrections and are proportional to $\Sigma_z^{\pm}$. Indeed, in the resonant limit, the first-order terms $\Delta_1^{\pm}(\tau_n) = -i\tau_n A/2\Sigma_y^{\pm}$ reproduce the RWA results [5] while the second-order terms $\Delta_2^{\pm}(\tau_n) = i\tau_n 3A^2/8\omega_d\Sigma_z^{\pm}$ correspond to the well-known Bloch-Siegert shift [12,70]. Transforming the propagator back to the laboratory frame via the identity $U_{\pm}(\tau_n) = U_0^{\pm}(\tau_n)U'_{\pm}(\tau_n)U_0^{\pm}(0)^{\dagger}$, we find

$$\begin{aligned} U_{\pm}(\tau_n) &= \exp(i\vartheta_{\pm}\Sigma_z^{\pm})[\cos(\xi_{\pm})\mathbb{1} - i\varepsilon_{\pm}\,\mathrm{sinc}(\xi_{\pm})\Sigma_z^{\pm}] \\ &\quad + i\sin(\xi_{\pm})\Sigma_y^{\pm} \\ &\approx \cos(\xi_{\pm})\exp\{i[\vartheta_{\pm} - \varepsilon_{\pm}\tan(\xi_{\pm})]\Sigma_z^{\pm}\} \\ &\quad + i\sin(\xi_{\pm})\Sigma_y^{\pm}, \end{aligned} \tag{31}$$

defining $\vartheta_{\pm} = \pi n\omega_{\pm}/\omega_d$. The approximate equality is valid for $\tan(\xi_{\pm})\varepsilon_{\pm} \ll 1$, and $\tan(x) = \tan(x)/x$.

B. Determining optimal drive parameters

To obtain the $\sqrt{\phi\mathrm{SWAP}}$ gate, we require

$$U_+(\tau_n) = \begin{pmatrix} \cos(\xi_+)e^{i(\vartheta_+ - \tan[\xi_+]\varepsilon_+)} & \sin(\xi_+) \\ -\sin(\xi_+) & \cos(\xi_+)e^{-i(\vartheta_+ - \tan[\xi_+]\varepsilon_+)} \end{pmatrix} \overset{!}{=} \begin{pmatrix} e^{i\alpha} & 0 \\ 0 & e^{-i\alpha} \end{pmatrix}, \tag{32}$$

$$U_-(\tau_n) = \begin{pmatrix} \cos(\xi_-)e^{i(\vartheta_- - \tan[\xi_-]\varepsilon_-)} & \sin(\xi_-) \\ -\sin(\xi_-) & \cos(\xi_-)e^{-i(\vartheta_- - \tan[\xi_-]\varepsilon_-)} \end{pmatrix} \overset{!}{=} \frac{1}{\sqrt{2}}\begin{pmatrix} e^{i\beta} & e^{i\gamma} \\ -e^{-i\gamma} & e^{-i\beta} \end{pmatrix}. \tag{33}$$

The solution for Eq. (32) is

$$\xi_+ = \frac{2A\omega_d}{\omega_d^2 - \omega_+^2}\sin\left(n\pi\frac{\omega_+}{\omega_d}\right) = p\pi, \quad p \in \mathbb{Z}, \tag{34}$$

which should be interpreted as an equation involving the unknowns A and ω_d. For any nonzero A, solutions to Eq. (34) for $p = 0$ are

$$\omega_d = n\omega_+/m, \quad (m = 1, 2, 3, \ldots, m \neq n). \tag{35}$$

For nonzero p, solutions (A and ω_d) can only be found by numerically solving the full transcendental Eq. (34). We find in the following that to satisfy Eq. (33), it is necessary to have the freedom of varying the drive amplitude A. Thus, we only consider the case $p = 0$. Setting $m = n$ is excluded in Eq. (35), as in this case the left-hand side of Eq. (34) does not vanish. However, this restriction is no issue, as—motivated by the drive frequency $\omega_d = \omega_-$ used to obtain the $\sqrt{i\mathrm{SWAP}}$ gate when the RWA is valid [5]—we do not consider on resonance driving of the $|\overline{00}\rangle \leftrightarrow |\overline{11}\rangle$

transition $\omega_d = \omega_+$. With ω_d given by Eq. (35), the expression for ε_+ simplifies to $\varepsilon_+ = A^2/\omega_d^2 \pi nm/1 - m^2$ and we satisfy Eq. (32) with the phase $\alpha = \vartheta_+ - \varepsilon_+$.

Considering now the requirement (33) for U_-, the solution is

$$\xi_- = \frac{2A\omega_d}{\omega_d^2 - \omega_-^2} \sin\left(n\pi \frac{\omega_-}{\omega_d}\right) = \pm\frac{\pi}{4} + \pi q, \quad q \in \mathbb{Z}, \tag{36}$$

where the $\pm$ indicates that the sign may be absorbed into the phases β and γ. We interpret Eq. (36) as an equation for the unknown A, as we have fixed ω_d previously. Solving for A yields

$$A = \pm\frac{\pi(\omega_d^2 - \omega_-^2)}{8\omega_d \sin(\pi n \frac{\omega_-}{\omega_d})}, \tag{37}$$

where we set $q = 0$ to minimize the magnitude of A. In general, the fraction on the right-hand side of Eq. (37) may be positive or negative, depending on n and the magnitude of ω_- relative to ω_d. Thus, we choose the sign of $\xi_- = \pm\pi/4$ based on which one yields a positive drive amplitude A. With the drive frequency and amplitude given by Eqs. (35) and (37), respectively, we satisfy Eq. (33) with phases $\beta = \vartheta_- - 4\varepsilon_-/\pi$ and $\gamma = 0$ or $\gamma = \pi$, depending on the sign of ξ_-.

The previous analysis only leaves us to choose the integers m and n [see Eq. (35)]. We make use of this freedom to limit the drive amplitude A in magnitude. Careful inspection of the removable singularity in Eq. (37) suggests the usage of a drive frequency ω_d near ω_-. This can be achieved by a combination of n and m such that their ratio n/m closely approximates ω_-/ω_+. The optimal choice of n must balance between mitigating the effects of T_1 and T_2 by keeping gate durations $2\pi n/\omega_d$ as short as possible and holding at bay unwanted population transfer incurred by strong drive amplitudes $A \sim 1/n$ (see Appendix C for details). With n and m specified as such, we construct the $\sqrt{\phi\text{SWAP}}$ gate allowing for the execution of a $\sqrt{i\text{SWAP}}$ gate when combined with single-qubit Z rotations.

C. Full-system numerical simulations

This realization of $\sqrt{i\text{SWAP}}$ reaches closed-system (open-system) fidelities as high as $F = 0.9996$ ($F = 0.9994$), which we obtain from numerical simulation of the full system as detailed in the following. The time evolution is based on the Hamiltonian $H(t) = H_0 + V + \sum_{\mu=a,b,c} h_\mu \delta\phi_\mu(t)$ [see Eqs. (1)–(2) as well as Eqs. (C1)–(C3) for the flux-activated terms]. The dc fluxes entering $H_0 + V$ are set to the off position [71], as is appropriate for performing single- and two-qubit gates. For numerical efficiency, $H(t)$ is expressed in the eigenbasis of the static Hamiltonian $H_0 + V$. The computational states of interest are the four lowest-energy states, with qubit frequencies $\omega_a'/2\pi = 58.1$ MHz, $\omega_b'/2\pi = 35.5$ MHz. Beyond these, we include up to 50 additional states in our simulations. For the parameters considered here, we have $\omega_-/\omega_+ = 0.24$; thus we choose $n/m = 1/4$, yielding $\omega_d/2\pi = 23.4$ MHz. Upon including the effects of decoherence, the choice $n = 2$ and thus $m = 8$, $A/2\pi = 2.9$ MHz optimizes the gate fidelity.

The full gate duration is $t_{\text{tot}} = 2\pi n/\omega_d + \max(t_{a1}, t_{b1}) + \max(t_{a2}, t_{b2})$, where $t_{\mu i} = -\theta_{\mu i}/\omega_\mu$. The equations for the times $t_{\mu i}$ are understood modulo 2π and the Z rotation angles are known in terms of the phases α, β, and γ [see Eq. (21)]. The angle θ_{b2} is a free parameter and is chosen to minimize the overall gate time by forcing the idle times after the $\sqrt{\phi\text{SWAP}}$ gate to coincide: $t_{a1} = t_{b1}$. For our parameters, we obtain $t_{\text{tot}} = 113$ ns, where $2\pi n/\omega d = 85$ ns and the single-qubit gates require 28 ns (see Fig. 8). For the initial state $|\overline{00}\rangle$, the population appreciably varies only during the single-qubit identity-gate segments [see Fig. 8(c)]. Meanwhile, for the state $|\overline{01}\rangle$, population transfer to the $|\overline{10}\rangle$ state occurs during the $\sqrt{\phi\text{SWAP}}$ portion of the gate [see Fig. 8(d)]. Closed-system simulations of this pulse sequence yield a gate fidelity of $F = 0.9996$ for achieving a $\sqrt{i\text{SWAP}}$ gate, calculated using Eq. (15), taking $d = 4$ and $U_T = \sqrt{i\text{SWAP}}$. Infidelities at the 10^{-4} level are likely due to residual effects from the higher-lying states that cause unwanted transitions in the computational subspace (for details, see Appendix C).

To include the detrimental effects of decoherence on gate fidelities, we numerically solve the Lindblad master equation

$$\frac{d\rho(t)}{dt} = -i[H(t), \rho(t)] + \sum_{\mu=a,b} [\Gamma_1^\mu \mathcal{D}(L_1^\mu)\rho(t) + \Gamma_\phi^\mu \mathcal{D}(L_\phi^\mu)\rho(t)], \tag{38}$$

where $\rho(t)$ is the system density matrix and

$$\mathcal{D}(L)\rho = L\rho L^\dagger - \frac{1}{2}\{L^\dagger L, \rho\},$$

is the standard form of the dissipator. The relevant jump operators L are

$$L_1^\mu = \bar{\sigma}_-^\mu, \quad L_\phi^\mu = \bar{\sigma}_z^\mu.$$

We neglect decoherence processes due to higher-lying states, noting that their occupation remains minimal throughout the duration of the pulse. We consider two sets of estimates for decoherence rates, one conservative, $\Gamma_\phi = 1/80\ \mu$s, $\Gamma_1 = 1/300\ \mu$s, and one optimistic, $\Gamma_\phi = 1/4000\ \mu$s, $\Gamma_1 = 1/1000\ \mu$s, both consistent with recent experiments [8,17]. At the conclusion of the gate, we project onto the computational subspace and perform numerical quantum process tomography [23,60,61,72] to

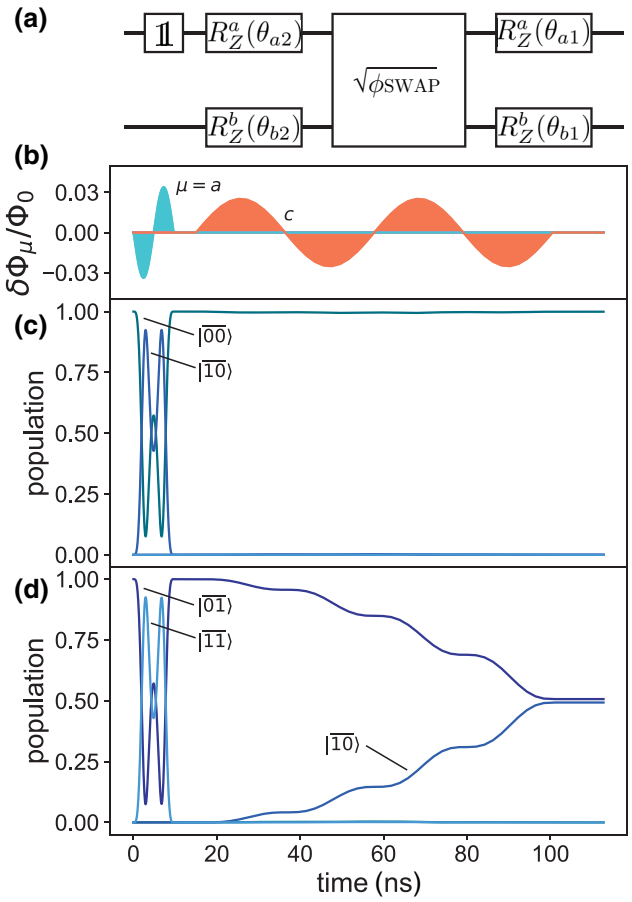

FIG. 8. A $\sqrt{i\text{SWAP}}$ gate composed of a $\sqrt{\phi\text{SWAP}}$ gate and corrective Z rotations. (a) A quantum circuit representation of the flux pulses shown in (b). The qubit flux $\delta\phi_a(t)$ (blue) is modulated to achieve the required identity operation, while the coupler flux $\delta\phi_c(t)$ (orange) is activated to entangle the qubits. Single-qubit Z rotations are obtained during the time spent idling. (c) The time evolution with the initial state $|\overline{00}\rangle$. The population transfer to the $|\overline{11}\rangle$ or other states is negligible during the $\sqrt{\phi\text{SWAP}}$ time window. (b) The time evolution for $|\overline{01}\rangle$ as the initial state. The $|\overline{01}\rangle$ and $|\overline{10}\rangle$ states exchange population during the segment when the coupler flux is nonzero. The closed-system fidelity of the $\sqrt{i\text{SWAP}}$ gate is $F = 0.9996$.

obtain the process matrix χ. The open-system gate fidelity is calculated using the formula [58,73–75]

$$F = \frac{d\,\mathrm{Tr}(\chi_T\chi) + \mathrm{Tr}(\chi)}{d+1}, \tag{39}$$

where d is the dimension of the relevant subspace and χ_T is the target process matrix. We obtain open-system gate fidelities of $F = 0.997$ and $F = 0.9994$ for the two cases of conservative and optimistic decoherence rate estimates, respectively [76].

V. DISCUSSION AND CONCLUSIONS

In this work, we propose a galvanic coupling scheme for fluxonium qubits in which XX coupling can be switched on and off while maintaining the qubits at their respective sweet spots. Motivated by record coherence times achieved with heavy-fluxonium qubits, we concentrate on operating at frequencies below approximately 200 MHz [8,17]. The magnitude of the drive strengths required to obtain fast gates invalidates RWA and makes it more natural to perform gates with reference to the laboratory frame. We present a protocol involving flux biasing and strong flux modulation that achieves a fast and high-fidelity $\sqrt{\phi\text{SWAP}}$ gate. To transform this into the more familiar $\sqrt{i\text{SWAP}}$ gate, we introduce variable-time identity gates. These gates, when combined with Z rotations, help us realize a $\sqrt{i\text{SWAP}}$ gate with fidelity $F > 0.999$. The fidelities are limited by incoherent errors as well as unwanted transitions in the computational subspace mediated by higher-lying states.

A crucial open question that warrants future research is how to achieve scalability in this fluxonium-based architecture. One may envision extending the device into a one-dimensional array of qubits and couplers. Generalization to two-dimensional arrays with increased qubit connectivity will require additional modifications due to the introduction of spurious superconducting loops that can themselves be threaded by external flux. If such a device can be successfully realized, it could be used to implement, e.g., an error-correcting surface code [77] or the multipath coupling architecture for fluxonium qubits described in Ref. [28], which requires inductive coupling strengths at the megahertz level.

ACKNOWLEDGMENTS

We thank Brian Baker, Ziwen Huang, and Yuan-Chi Yang for helpful discussions. D.K.W. acknowledges support from the Army Research Office (ARO) through a QuaCGR Fellowship. This research was funded by the ARO under Grant No. W911NF-19-10016. This work has relied on multiple open-source software packages, including MATPLOTLIB [78], NumPy [79], QuTiP [60,61], SciPy [80], and SCQUBITS [59].

APPENDIX A: FULL-CIRCUIT ANALYSIS

In this appendix, we construct the Lagrangian and Hamiltonian of the full circuit shown in Fig. 9, allowing for disorder in circuit parameters. We follow the method of Vool and Devoret [81] to construct the circuit Lagrangian, yielding

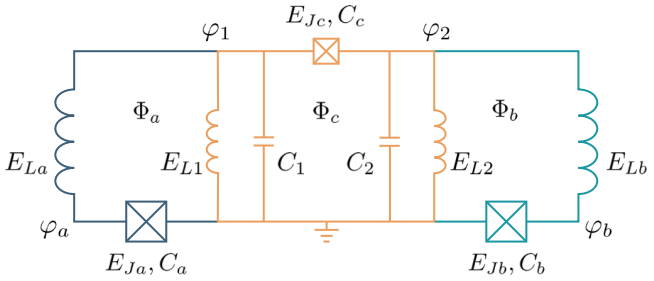

FIG. 9. A schematic of the full circuit, accounting for parameter disorder.

$$\mathcal{L} = \frac{\Phi_0^2}{2(2\pi)^2}\left(\sum_{\mu=a,b} C_\mu \dot{\varphi}_\mu^2 + \sum_{i=1,2} C_i \dot{\varphi}_i^2 + C_c[\dot{\varphi}_1 - \dot{\varphi}_2]^2\right) - \frac{1}{2}E_{La}(\varphi_a - \varphi_1)^2 - \frac{1}{2}E_{Lb}(\varphi_b - \varphi_2)^2 - \frac{1}{2}\sum_{i=1,2} E_{Li}\varphi_i^2 + \sum_{\mu=a,b} E_{J\mu}\cos(\varphi_\mu + \phi_\mu) + E_{Jc}\cos(\varphi_1 - \varphi_2 + \phi_c),$$

with node variables and circuit parameters as shown in Fig. 9. We consider the case of small deviations from otherwise pairwise-equivalent qubit inductors E_{La} and E_{Lb}, coupler inductors E_{L1} and E_{L2}, and stray capacitances C_1 and C_2. In the absence of parameter disorder, the coupler modes $\theta_\pm = \varphi_1 \pm \varphi_2$ decouple, simplifying the analysis (though we show below that small parameter disorder is not expected to significantly impact device performance). Using these variables, the Lagrangian becomes

$$\begin{aligned}\mathcal{L} = {} & \frac{1}{2}\left(\frac{\Phi_0}{2\pi}\right)^2\left(\sum_{\mu=a,b} C_\mu \dot{\varphi}_\mu^2 + \frac{1}{2}C\dot{\theta}_+^2 + [C_c + \frac{1}{2}C]\dot{\theta}_-^2 + \frac{1}{2}C\,dC\,\dot{\theta}_+\dot{\theta}_-\right) \\ & + \sum_{\mu=a,b}(E_{J\mu}\cos[\varphi_\mu + \phi_\mu] - \frac{1}{2}E_{L\mu}\varphi_\mu^2) \\ & - \sum_{i=\pm}\frac{1}{2}E_{Lc}\theta_i^2 + E_{Jc}\cos(\theta_- + \phi_c) \\ & - \frac{1}{4}(E_L dE_L + E_L' dE_L')\theta_+\theta_- \\ & + \frac{1}{2}E_{La}\varphi_a(\theta_+ + \theta_-) + \frac{1}{2}E_{Lb}\varphi_b(\theta_+ - \theta_-), \end{aligned} \tag{A1}$$

where $E_{Lc} = \frac{1}{2}(E_L + E_L')$ and we introduce notation for the average and relative deviation of the qubit inductors $E_L = \frac{1}{2}(E_{La} + E_{Lb})$ and $dE_L = (E_{La} - E_{Lb})/E_L$, the coupler inductors $E_L' = \frac{1}{2}(E_{L1} + E_{L2})$ and $dE_L' = (E_{L1} - E_{L2})/E_L'$, and the stray capacitances $C = \frac{1}{2}(C_1 + C_2)$ and $dC = (C_1 - C_2)/C$. We perform the Legendre transform to obtain the Hamiltonian and promote our variables to noncommuting operators obeying the commutation relations $[\varphi_\mu, n_\mu] = i$ for $\mu = a, b$ and $[\theta_j, n_j] = i$ for $j = \pm$. The Hamiltonian is $H = H_0 + V + H_{\rm dis}$, where

$$\begin{aligned} H_0 = {} & \sum_{\mu=a,b}[4E_{C\mu}n_\mu^2 + \frac{1}{2}E_{L\mu}\varphi_\mu^2 - E_{J\mu}\cos(\varphi_\mu + \pi)] \\ & + 4E_{C-}n_-^2 + \frac{1}{2}E_{Lc}\theta_-^2 - E_{Jc}\cos(\theta_- + \phi_c) \\ & + 4E_{C+}n_+^2 + \frac{1}{2}E_{Lc}\theta_+^2, \end{aligned} \tag{A2}$$

$$\begin{aligned} V = {} & -\sum_{\mu=a,b}\frac{E_{L\mu}}{2}\varphi_\mu[\theta_+ + (-1)^\mu\theta_-] \\ & + \sum_{\mu=a,b}\frac{E_{L\mu}}{2}\delta\phi^\mu[-2\varphi_\mu + \theta_+ + (-1)^\mu\theta_-], \end{aligned} \tag{A3}$$

$$\begin{aligned} H_{\rm dis} = {} & \frac{1}{4}(E_L dE_L + E_L' dE_L')\theta_+\theta_- \\ & - 4E_{C-}dC n_+ n_- + \mathcal{O}(dC^2). \end{aligned} \tag{A4}$$

The charging-energy definitions introduced above are given in the main text and H_0, V, and $H_{\rm dis}$ refer to the bare, coupling, and disorder Hamiltonians, respectively. We neglect higher-order disorder contributions proportional to dC^2 on the assumption that disorder is small. Additionally, we isolate the qubit flux shift away from the sweet spot $\delta\phi_\mu = \phi_\mu - \pi$ and perform the variable transformation $\varphi_\mu \to \varphi_\mu - \delta\phi_\mu$.

APPENDIX B: SCHRIEFFER-WOLFF TRANSFORMATION

In this appendix, we derive the second-order effective Hamiltonian describing the qubit-qubit interaction that is dispersively mediated by the tunable coupler. First, we consider the symmetric case $H_{\rm dis} = 0$. Later, we relax this assumption and allow for parameter disorder.

1. Effective Hamiltonian without parameter disorder

We separate the Hilbert space into a low- and a high-energy subspace defined by the respective projectors:

$$P = \sum_{\ell,m\in\{0,1\}} |\ell_a, m_b, 0_-, 0_+\rangle\langle \ell_a, m_b, 0_-, 0_+|, \tag{B1}$$

$$Q = \mathbb{1} - P. \tag{B2}$$

We define the states $|\ell_a, m_b, n_-, p_+\rangle$ that are eigenstates of the bare Hamiltonian H_0 with eigenenergies $E_\ell^a + E_m^b + E_n^- + p\omega_+$. The perturbation V couples states within the same subspace, as well as states in separate subspaces. We utilize a Schrieffer-Wolff transformation [5,46–48] e^{-S} with an anti-Hermitian generator S to decouple the

low- and high-energy subspaces order by order. To carry out the transformation, the effective Hamiltonian $H_{\text{eff}} = Pe^{S}He^{-S}P$ and generator S are expanded as

$$H_{\text{eff}} = H^{(0)} + H^{(1)} + H^{(2)} + \cdots, \tag{B3}$$

$$S = S^{(1)} + S^{(2)} + \cdots. \tag{B4}$$

We then collect terms of the same order and enforce both that the effective Hamiltonian is block diagonal and that the generator is block off diagonal.

The zeroth- and first-order contributions to the effective Hamiltonian in the computational subspace (neglecting constant terms) are found by applying the projector P onto H_0 and V, respectively [5,46–48]:

$$H^{(0)} = PH_0P = -\sum_{\mu=a,b} \frac{\omega_\mu}{2}\sigma_z^\mu, \tag{B5}$$

$$H^{(1)} = PVP = -\sum_{\mu=a,b} \Omega_\mu \sigma_x^\mu, \tag{B6}$$

where $\omega_\mu = E_1^\mu - E_0^\mu$ and

$$\Omega_\mu = E_L \langle 0_\mu|\varphi_\mu|1_\mu\rangle \left[\delta\phi_\mu + (-1)^\mu \frac{\langle 0_\mu|\theta_-|0_\mu\rangle}{2}\right]. \tag{B7}$$

The Pauli matrices are defined as, e.g., $\sigma_x^a = \sum_{m=0,1} |0_a, m_b, 0_-, 0_+\rangle\langle 1_a, m_b, 0_-, 0_+| + \text{H.c.}$

Calculation of the second-order contribution $H^{(2)}$ to the effective Hamiltonian is facilitated by the first-order generator $S^{(1)}$. The expression for the matrix elements of $S^{(1)}$ is well known [5] and we obtain

$$S^{(1)} = \sum_{\substack{\mu=a,b\\ j=0,1}} \left({\sum_{j',n}}' (-1)^{\mu+1} \epsilon^{\mu,(1)}_{jj',n} |j_\mu, 0_-\rangle\langle j'_\mu, n_-| - \sum_{j'} \eta^{\mu,(1)}_{jj'} |j_\mu, 0_+\rangle\langle j'_\mu, 1_+| \right) - \text{H.c.}, \tag{B8}$$

defining the small parameters

$$\epsilon^{\mu,(1)}_{jj',n} = \frac{g^\mu_{jj',0n}}{E^\mu_{jj'} - E^-_{n0}}, \quad \eta^{\mu,(1)}_{jj'} = \frac{G^\mu_{jj'}}{E^\mu_{jj'} - \omega_+}, \tag{B9}$$

where $E^\mu_{jk} = E^\mu_j - E^\mu_k$, $\mu = a, b, -$, and

$$g^\mu_{jj',0n} = \frac{E_L}{2}\langle 0_-|\theta_-|n_-\rangle\langle j_\mu|\varphi_\mu|j'_\mu\rangle, \tag{B10}$$

$$G^\mu_{jj'} = \frac{E_L}{2}\left(\frac{2E_{C+}}{E_{Lc}}\right)^{1/4} \langle j_\mu|\varphi_\mu|j'_\mu\rangle. \tag{B11}$$

We introduce annihilation and creation operators $a_+, a_+^\dagger$ for the coupler θ_+ mode via $\theta_+ = \ell_{\text{osc}}/\sqrt{2}(a_+ + a_+^\dagger)$ and $\ell_{\text{osc}} = (8E_{C+}/E_{Lc})^{1/4}$ is the oscillator length. The primed sum in Eq. (B8) indicates that n is allowed to be zero if $j' \geq 2$, acknowledging that the perturbation V can couple computational states to higher-lying states of the qubit fluxoniums without exciting the coupler θ_- mode. We neglect contributions proportional to $\delta\phi_\mu$ in Eq. (B8), as they are comparatively small.

Using the first-order generator, we can compute the second-order effective Hamiltonian in the low-energy subspace via the formula $H^{(2)} = \frac{1}{2}P[S^{(1)}, V]P$ [5,46–48], yielding

$$H^{(2)} = -\sum_{\mu=a,b} \frac{\chi_\mu}{2}\sigma_z^\mu + J\sigma_x^a\sigma_x^b, \tag{B12}$$

where we define $\chi_\mu = \chi_1^\mu - \chi_0^\mu$ and neglect global energy shifts. The qubit-frequency renormalization coefficients are

$$\chi_j^\mu = -\sum_{j'} \left({\sum_n}' \frac{|g^\mu_{jj',n0}|^2}{\delta^\mu_{jj',n}} + \frac{|G^\mu_{jj'}|^2}{\Delta^\mu_{jj'}} \right), \tag{B13}$$

defining the energy denominators $\delta^\mu_{jj',n} = E^-_{n0} - E^\mu_{jj'}$ and $\Delta^\mu_{jj'} = \omega_+ - E^\mu_{jj'}$. The two-qubit interaction strength is

$$\begin{aligned} J &= \sum_{n\geq 1} \frac{g^a_{01,0n} g^b_{01,0n}}{2} \left(\frac{1}{\delta^a_{01,n}} + \frac{1}{\delta^a_{10,n}} + \frac{1}{\delta^b_{01,n}} + \frac{1}{\delta^b_{10,n}} \right) \\ &\quad - \frac{G^a_{01}G^b_{01}}{2} \left(\frac{1}{\Delta^a_{01}} + \frac{1}{\Delta^a_{10}} + \frac{1}{\Delta^b_{01}} + \frac{1}{\Delta^b_{10}} \right) \\ &= J_- - J_+, \end{aligned} \tag{B14}$$

implicitly defining $J_\pm$. Thus, the effective Hamiltonian in the computational subspace up to second order is

$$H_{\text{eff}} = -\sum_{\mu=a,b} \frac{\omega'_\mu}{2}\sigma_z^\mu + J\sigma_x^a\sigma_x^b - \sum_{\mu=a,b} \Omega_\mu \sigma_x^\mu, \tag{B15}$$

where $\omega'_\mu = \omega_\mu + \chi_\mu$.

It is instructive to consider J in the limit where the coupler excitation energies dominate over those of the qubits. In this case, we find

$$\begin{aligned} J &= \frac{E_L^2}{2}\langle 0_a|\varphi_a|1_a\rangle\langle 0_b|\varphi_b|1_b\rangle \\ &\quad \times \left(\sum_{n\geq 1} \frac{|\langle 0_-|\theta_-|n_-\rangle|^2}{E^-_{n0}} - \frac{1}{2E_{Lc}} \right) + \mathcal{O}\left(\frac{E^{a,b}_{01}}{\omega_+}, \frac{E^{a,b}_{01}}{E^-_{10}} \right). \end{aligned} \tag{B16}$$

Thus the tunability of J discussed in the main text arises from the dependence of the matrix elements $\langle 0_-|\theta_-|n_-\rangle$ and energies E^-_{n0} on the coupler flux. In this limit, the static contribution to J due to the harmonic coupler θ_+ mode is insensitive to the value of E_{C+}.

2. Effective Hamiltonian in the presence of disorder

We now consider how disorder in circuit parameters modifies the form of the effective Hamiltonian in Eq. (B15). This disorder could arise, for example, from fabrication imperfections. We show below that up to second order, inductive disorder merely results in a modification to Eq. (B7), while capacitive disorder does not contribute.

From Eq. (A3), we see that inductive asymmetry adds a disorder term to the Hamiltonian

$$H_{\rm ind} = \frac{1}{4}(E_L dE_L + E'_L dE'_L)\theta_+\theta_-. \tag{B17}$$

If we assume that the relative deviations are small compared with unity, it is justified to add this term to V and treat it perturbatively. Observe that on the one hand, for virtual transitions mediated by this term, the excitation number of either qubit cannot change. On the other hand, the excitation number of the coupler θ_+ mode must change. Thus, the first-order contributions vanish and the only second-order terms that contribute beyond a global energy shift are

$$H^{(2)}_{\rm ind} = -\frac{1}{2}\sum_{\mu=a,b} g_{\rm ind}(\eta^{\mu}_{01} + \eta^{\mu}_{10})\sigma^{\mu}_x, \tag{B18}$$

where we define

$$g_{\rm ind} = \frac{\ell_{\rm osc}}{4\sqrt{2}}(E_L dE_L + E'_L dE'_L)\langle 0_-|\theta_-|0_-\rangle. \tag{B19}$$

Thus, up to second order, disorder in the inductors serves only to modify the expressions for the coefficients Ω_μ. As discussed in the main text, this amounts to a shift in the sweet-spot location of each qubit and can be canceled by a corresponding shift of the static qubit fluxes. Thus, small disorder in either the qubit inductors or the coupler inductors does not adversely affect device performance.

We now turn our attention to capacitive disorder $C_1 \neq C_2$ (disorder in the qubit capacitances poses no issue, as the qubits remain decoupled from all other degrees of freedom in the kinetic part of the Hamiltonian). In this case, we proceed as before and treat perturbatively the capacitive-disorder term

$$H_{\rm cap} = -4E_{C-} dC n_+ n_-. \tag{B20}$$

Consider the relation between the phase and charge matrix elements in fluxonium [27],

$$\langle j_-|n_-|k_-\rangle = i\frac{E^-_{jk}}{8E_{C-}}\langle j_-|\theta_-|k_-\rangle, \tag{B21}$$

and observe that the charge matrix element vanishes if $j = k$. Thus, any virtual transition mediated by the perturbation (B20) must excite both the coupler θ_- mode and the coupler θ_+ mode and thus does not contribute at second order beyond a global energy shift.

APPENDIX C: DRIVE OPERATORS

In this appendix, we calculate the matrix elements and consider the effects of the relevant drive operators activated by time-dependent flux drives. Allocating the time-dependent flux in the same way as for static flux generally introduces terms proportional to the time derivative of the external flux [82]. Imposing the constraint that these terms should not appear implies a specific grouping of the flux in the full Hamiltonian H. For our parameters, we find to a good approximation that the ac qubit fluxes are allocated to their respective inductors and the ac coupler flux is spread across all four inductors. We first decompose the external fluxes into static $\bar{\phi}_\mu$ and time-dependent $\delta\phi_\mu(t)$ components, where $\bar{\phi}_\mu$ are the dc-flux values at the off position. The ac qubit fluxes are already properly allocated, while the appropriate grouping of the coupler flux is obtained via $\theta_- \to \theta_- - \delta\phi_c(t)$. The full time-dependent Hamiltonian is thus $H(t) = H_0 + V + h_a\delta\phi_a(t) + h_b\delta\phi_b(t) + h_c\delta\phi_c(t)$, where

$$h_a = \frac{E_L}{2}(-2\varphi_a + \theta_+ + \theta_-), \tag{C1}$$

$$h_b = \frac{E_L}{2}(-2\varphi_b + \theta_+ - \theta_-), \tag{C2}$$

$$h_c = \left(\frac{E_L}{2}\varphi_a - \frac{E_L}{2}\varphi_b - E_{Lc}\theta_-\right). \tag{C3}$$

Matrix elements of the operators h_μ with respect to eigenstates of the static Hamiltonian $H_{\rm st} = H_0 + V$ determine the time evolution, once the time-dependent drives $\delta\phi_\mu(t)$ are specified. The Schrieffer-Wolff transformation allows us to define new basis states that are approximate eigenstates of $H_{\rm st}$ and thus perturbatively calculate these matrix elements.

The leading-order contributions to select matrix elements of the drive operators h_μ occur at second order. Thus, to include all relevant corrections to the wave functions that contribute to these matrix elements, we calculate the second-order generator $S^{(2)}$ associated with the Schrieffer-Wolff transformation discussed in Appendix B. To simplify the calculation, we ignore all contributions from the coupler θ_+ mode due to the inequality $|\eta| < |\epsilon|$ in the parameter regime of interest, yielding [5,48]

$$S^{(2)} = \sum_{\substack{\mu=a,b\\ j=0,1}}\sum_{j',n}{}' \epsilon^{\mu,(2)}_{jj',n}|j_\mu, 0_-\rangle\langle j'_\mu, n_-| + \sum_{j,k=0,1}\sum_{j',k',n}{}' \epsilon^{ab,(2)}_{jj',kk',n}|j_a, k_b, 0_-\rangle\langle j'_a, k'_b, n_-| - \text{H.c.} \tag{C4}$$

where we define

$$\epsilon^{\mu,(2)}_{jj',n} = -\sum_{j''=0,1} \frac{g^{\mu}_{jj'',00} g^{\mu}_{j''j',0n}}{(E^{\mu}_{jj'} - E^{-}_{n0})(E^{\mu}_{j''j'} - E^{-}_{n0})} + {\sum_{j'',n}}' \frac{g^{\mu}_{jj'',0n'} g^{\mu}_{j''j',n'n}}{(E^{\mu}_{jj''} - E^{-}_{n'0})(E^{\mu}_{jj'} - E^{-}_{n0})},$$

$$\epsilon^{ab,(2)}_{jj',kk',n} = \sum_{\substack{\mu,\nu=a,b \\ \mu\neq\nu}} \left[\frac{g^{\mu}_{jj',00} g^{\nu}_{kk',0n}}{(E^{\mu}_{jj'} + E^{\nu}_{kk'} - E^{-}_{n0})(E^{\nu}_{kk'} - E^{-}_{n0})} - {\sum_{n'}}' \frac{g^{\mu}_{jj',0n'} g^{\nu}_{kk',n'n}}{(E^{\mu}_{jj'} - E^{-}_{n'0})(E^{\mu}_{jj'} + E^{\nu}_{kk'} - E^{-}_{n0})} \right].$$

At the off position, the effective Hamiltonian $H_{\text{eff}} = -\omega'_a/2\sigma^a_z - \omega'_b/2\sigma^b_z$ (ignoring third-order contributions to the effective Hamiltonian) is diagonal in the basis of the bare computational states $|\ell_a, m_b, 0, 0\rangle, \ell, m \in \{0, 1\}$. Assuming that the qubit frequencies are not on resonance $\omega'_a \neq \omega'_b$, the dressed eigenstates are

$$|\overline{\ell_a, m_b, 0_-, 0_+}\rangle = e^{-S}|\ell_a, m_b, 0_-, 0_+\rangle = \left[\mathbb{1} - S^{(1)} - S^{(2)} + \frac{1}{2}(S^{(1)})^2\right]|\ell_a, m_b, 0_-, 0_+\rangle, \quad \text{(C5)}$$

up to second order. With the dressed eigenstates now written in terms of bare states, we may compute the matrix elements of the operators h_μ associated with the ac flux drives.

1. Qubit-flux drive operators

Experimentally, the amplitude of an ac flux drive will typically be no larger than $\delta\Phi_\mu \leq 0.1\Phi_0$ [8]. In this case, we check that transitions to higher-lying states mediated by the drive operators h_a, h_b are suppressed. Thus, we need only consider matrix elements of these operators in the computational subspace. Using the expression in Eq. (C5) for the dressed states given in terms of the bare states, we find

$$\langle\overline{\ell m}|h_a|\overline{\ell m}\rangle/E_L = 2\sum_{\ell'\geq 2}\langle\ell_a|\varphi_a|\ell'_a\rangle\epsilon^{a,(1)}_{\ell\ell',0} + \frac{1}{2}\langle 0_-|\theta_-|0_-\rangle, \quad \text{(C6)}$$

$$\langle\overline{\ell m}|h_a|\overline{\ell+1 m}\rangle/E_L = -\langle 0_a|\varphi_a|1_a\rangle - \frac{1}{2}\sum_{n\geq 1}\langle 0_-|\theta_-|n_-\rangle(\epsilon^{a,(1)}_{01,n} + \epsilon^{a,(1)}_{10,n}) - \frac{1}{2}\frac{\ell_{\text{osc}}}{\sqrt{2}}(\eta^{a,(1)}_{01} + \eta^{a,(1)}_{10}), \quad \text{(C7)}$$

$$\langle\overline{\ell m}|h_a|\overline{\ell m+1}\rangle/E_L = -\frac{1}{2}\frac{\ell_{\text{osc}}}{\sqrt{2}}(\eta^{b,(1)}_{01} + \eta^{b,(1)}_{10}) + \frac{1}{2}\sum_{n\geq 1}\langle 0_-|\theta_-|n_-\rangle(\epsilon^{b,(1)}_{01,n} + \epsilon^{b,(1)}_{10,n})], \quad \text{(C8)}$$

$$\begin{aligned}\langle\overline{\ell m}|h_a|\overline{\ell+1 m+1}\rangle/(E_L/2) = &-\sum_{n,n'\geq 1}(\epsilon^{a,(1)}_{\ell\ell+1,n}\epsilon^{b,(1)}_{m+1m,n'} + \epsilon^{a,(1)}_{\ell+1\ell,n}\epsilon^{b,(1)}_{mm+1,n'})\langle n_-|\theta_-|n'_-\rangle \\ &+\sum_{n\geq 1}(\epsilon^{ab,(2)}_{\ell\ell+1,mm+1,n} + \epsilon^{ab,(2)}_{\ell+1\ell,m+1m,n})\langle 0_-|\theta_-|n_-\rangle \\ &+\sum_{n\geq 1}(\epsilon^{a,(1)}_{\ell\ell+1,n}\epsilon^{b,(1)}_{m+1m,n} + \epsilon^{a,(1)}_{\ell+1\ell,n}\epsilon^{b,(1)}_{mm+1,n})\langle 0_-|\theta_-|0_-\rangle, \end{aligned} \quad \text{(C9)}$$

where we introduce the shorthand $|\overline{\ell, m}\rangle \equiv |\overline{\ell_a, m_b, 0_-, 0_+}\rangle$ for states in the computational subspace and the labels are understood modulo 2. In Eqs. (C6)–(C8), second-order contributions are small and can be neglected, while in Eq. (C9), the leading-order contributions are at second order. These analytical approximations indicate that in the computational subspace and at the off position, the operator h_a simplifies dramatically to leading order to $\Omega^a_{\text{ac}}\bar{\sigma}^a_x$. For example, the matrix element in Eq. (C8) vanishes at the off position by definition [see Eq. (B14)].

Further explicit verification of the form of h_a is tedious and is omitted. We find excellent agreement between the semianalytic formulas and exact results: for the parameters considered here, we obtain $|\Omega^a_{\text{ac}}|/h = 558, 561$ MHz using Eqs. (C6)–(C9) and numerics, respectively. The coefficients associated with all other operators (aside from the irrelevant identity) in the decomposition of h_a are of the order of 2 h MHz or smaller in absolute value, as calculated both from the semianalytic formulas and exact results.

2. Coupler-flux drive operator

The operator h_c activated by coupler-flux modulation induces both wanted and unwanted transitions in the computational subspace. The latter proceed through virtual excitations of higher-lying states. We analyze both types of transitions in the following.

a. Computational-subspace matrix elements

The matrix elements of h_c governing the wanted transitions can be obtained within second-order perturbation theory using Eq. (C5):

$$\langle\overline{\ell m}|h_c|\overline{\ell m}\rangle = -E_{Lc}\langle 0_-|\theta_-|0_-\rangle - E_L\sum_{\ell'\geq 2}\langle \ell_a|\varphi_a|\ell'_a\rangle\epsilon^{a,(1)}_{\ell\ell',0} - E_L\sum_{m'\geq 2}\langle m_b|\varphi_b|m'_b\rangle\epsilon^{b,(1)}_{mm',0}, \tag{C10}$$

$$\langle\overline{\ell m}|h_c|\overline{\ell+1 m}\rangle = \frac{E_L}{2}\langle 0_a|\varphi_a|1_a\rangle + E_{Lc}\sum_{n\geq 1}\langle 0_-|\theta_-|n_-\rangle(\epsilon^{a,(1)}_{01,n} + \epsilon^{a,(1)}_{10,n}), \tag{C11}$$

$$\langle\overline{\ell m}|h_c|\overline{\ell m+1}\rangle = -\frac{E_L}{2}\langle 0_b|\varphi_b|1_b\rangle - E_{Lc}\sum_{n\geq 1}\langle 0_-|\theta_-|n_-\rangle(\epsilon^{b,(1)}_{01,n} + \epsilon^{b,(1)}_{10,n}), \tag{C12}$$

$$\langle\overline{\ell m}|h_c|\overline{\ell+1 m+1}\rangle = -\frac{E_{Lc}}{E_L/2}\langle\overline{\ell m}|h_a|\overline{\ell+1 m+1}\rangle. \tag{C13}$$

At the off position h_c can be simplified to

$$h_c = J_{\rm ac}\bar{\sigma}^a_x\bar{\sigma}^b_x, \tag{C14}$$

where we define the ac XX coupling strength

$$J_{\rm ac} = \frac{1}{2}(\langle\overline{00}|h_c|\overline{11}\rangle + \langle\overline{01}|h_c|\overline{10}\rangle). \tag{C15}$$

For our parameters, we obtain $|J_{\rm ac}|/h = 14.3$ and 18.3 MHz using the semianalytic formulas Eqs. (C10)–(C13) and exact numerics, respectively. We have checked that the semianalytic results agree with exact numerics in the limit of large E_{Lc}, where the interaction becomes more dispersive.

b. Virtual transitions involving higher-lying states

The full analysis of time evolution when modulating the coupler flux (Sec. IV) requires consideration of higher-lying states. These states outside the computational subspace, while largely remaining unoccupied, participate as virtual intermediate states in unwanted transitions. We estimate the amount of population transfer between the states $|i\rangle = |\overline{\ell_a, m_b, 0_-, 0_+}\rangle$ and $|f\rangle = |\overline{\ell'_a, m'_b, 0_-, 0_+}\rangle$ with $i \neq f$ at the conclusion of the gate $t = 2\pi n/\omega_d$ using time-dependent perturbation theory up to second order [83]:

$$T_{\ell m\to\ell' m'} = \left|\frac{i\langle f|\delta\phi_c h_c|i\rangle\omega_d}{E_{fi}^2 - \omega_d^2}(1 - e^{2\pi i n E_{fi}/\omega_d}) + \sum_v \frac{\omega_d^2\langle f|\delta\phi_c h_c|v\rangle\langle v|\delta\phi_c h_c|i\rangle}{E_{vi}^2 - \omega_d^2}\right.$$
$$\left. \times\left(\frac{[2E_{vi} + E_{fi}][1 - e^{2\pi i n E_{fi}/\omega_d}]}{E_{fi}[E_{fi}^2 - 4\omega_d^2]} - \frac{1 - e^{2\pi i n E_{fv}/\omega_d}}{E_{fv}^2 - \omega_d^2}\right)\right|^2, \tag{C16}$$

where the sum on v is over virtual intermediate states $|v\rangle = |\overline{\ell''_a, m''_b, p_-, q_+}\rangle$ and we define $E_{fv} = E_{\overline{\ell' m' 00}} - E_{\overline{\ell'' m'' pq}}$, etc. The top line of Eq. (C16) represents direct transitions between the states $|i\rangle$ and $|f\rangle$, occurring for nonzero $\langle f|h_c|i\rangle$ (e.g., $|i\rangle = |\overline{0_a, 1_b, 0_-, 0_+}\rangle$ and $|f\rangle = |\overline{1_a, 0_b, 0_-, 0_+}\rangle$). These are the wanted transitions discussed previously. The second and third lines of Eq. (C16) are the second-order contributions and allow for unwanted transitions. Based on numerical calculation of the matrix elements of h_c between the computational states and higher-lying states, we find that the four states $|v\rangle = |\overline{\ell_a, m_b, 1_-, 0_+}\rangle$, $\ell, m \in \{0, 1\}$ with an excitation in the θ_- mode dominate the sum on v (see Fig. 10). (Note that this virtual process is heavily suppressed in the context of qubit-flux drives, due to the comparatively small coefficient $E_L/2 \ll E_{Lc}$ multiplying the operator θ_- in h_a).

These transitions mediated by the higher-lying states can significantly degrade gate fidelities. Indeed, attempting to implement the $\sqrt{\phi\rm SWAP}$ gate with only a single drive period leads to poor fidelities $F < 0.9$ due to the unwanted transitions. Slowing down the gate by utilizing two drive periods as in Sec. IV mitigates this issue in large part (the infidelities are on the order of 10^{-4}) by reducing the required drive amplitude. It is an interesting avenue for further research to investigate means for overcoming

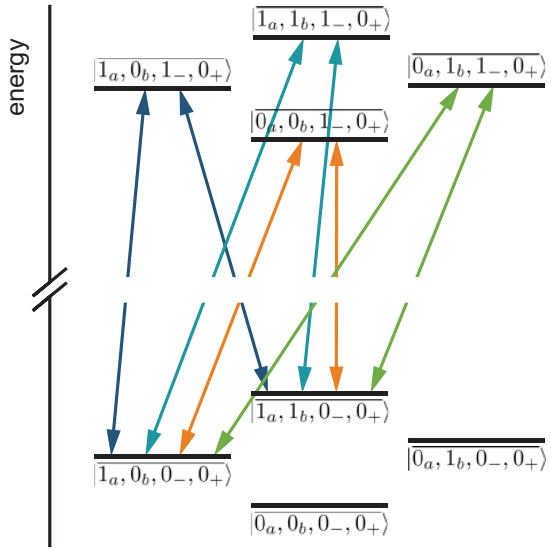

FIG. 10. A schematic of the unwanted transitions in the computational subspace. These transitions are due to virtual excitations of the higher-lying states $|\overline{\ell_a, m_b, 1_-, 0_+}\rangle, \ell, m \in \{0, 1\}$ mediated by the drive operator h_c. As an example, we show the four perturbative paths contributing to the undesired transition $|\overline{1_a, 0_b, 0_-, 0_+}\rangle \leftrightarrow |\overline{1_a, 1_b, 0_-, 0_+}\rangle$.

this limitation on $\delta\phi_c$ to achieve faster gate times without sacrificing fidelity.

[1] J. Preskill, Quantum computing in the NISQ era and beyond, Quantum **2**, 79 (2018).

[2] V. Negîrneac, H. Ali, N. Muthusubramanian, F. Battistel, R. Sagastizabal, M. S. Moreira, J. F. Marques, W. J. Vlothuizen, M. Beekman, C. Zachariadis, N. Haider, A. Bruno, and L. DiCarlo, High-Fidelity Controlled-*Z* Gate with Maximal Intermediate Leakage Operating at the Speed Limit in a Superconducting Quantum Processor, Phys. Rev. Lett. **126**, 220502 (2021).

[3] E. Dogan, D. Rosenstock, L. L. Guevel, H. Xiong, R. A. Mencia, A. Somoroff, K. N. Nesterov, M. G. Vavilov, V. E. Manucharyan, and C. Wang, Demonstration of the two-fluxonium cross-resonance gate (2022), ArXiv:2204.11829.

[4] B. Foxen, C. Neill, A. Dunsworth, P. Roushan, B. Chiaro, A. Megrant, J. Kelly, Z. Chen, K. Satzinger, and R. Barends, *et al.*, Demonstrating a Continuous Set of Two-Qubit Gates for Near-Term Quantum Algorithms, Phys. Rev. Lett. **125**, 120504 (2020).

[5] A. Blais, A. L. Grimsmo, S. M. Girvin, and A. Wallraff, Circuit quantum electrodynamics, Rev. Mod. Phys. **93**, 025005 (2021).

[6] N. Earnest, S. Chakram, Y. Lu, N. Irons, R. K. Naik, N. Leung, L. Ocola, D. A. Czaplewski, B. Baker, J. Lawrence, J. Koch, and D. I. Schuster, Realization of a Λ System with Metastable States of a Capacitively Shunted Fluxonium, Phys. Rev. Lett. **120**, 150504 (2018).

[7] Y.-H. Lin, L. B. Nguyen, N. Grabon, J. San Miguel, N. Pankratova, and V. E. Manucharyan, Demonstration of Protection of a Superconducting Qubit from Energy Decay, Phys. Rev. Lett. **120**, 150503 (2018).

[8] H. Zhang, S. Chakram, T. Roy, N. Earnest, Y. Lu, Z. Huang, D. K. Weiss, J. Koch, and D. I. Schuster, Universal Fast-Flux Control of a Coherent, Low-Frequency Qubit, Phys. Rev. X **11**, 011010 (2021).

[9] W. Magnus, On the exponential solution of differential equations for a linear operator, Commun. Pure Appl. Math. **7**, 649 (1954).

[10] S. Blanes, F. Casas, J. A. Oteo, and J. Ros, The Magnus expansion and some of its applications, Phys. Rep. **470**, 151 (2009).

[11] R. M. Wilcox, Exponential operators and parameter differentiation in quantum physics, J. Math. Phys. **8**, 962 (1967).

[12] D. Zeuch, F. Hassler, J. J. Slim, and D. P. DiVincenzo, Exact rotating wave approximation, Ann. Phys. **423**, 168327 (2020).

[13] D. L. Campbell, Y. P. Shim, B. Kannan, R. Winik, D. K. Kim, A. Melville, B. M. Niedzielski, J. L. Yoder, C. Tahan, S. Gustavsson, and W. D. Oliver, Universal Nonadiabatic Control of Small-Gap Superconducting Qubits, Phys. Rev. X **10**, 041051 (2020).

[14] Y. C. Yang, S. N. Coppersmith, and M. Friesen, Achieving high-fidelity single-qubit gates in a strongly driven silicon-quantum-dot hybrid qubit, Phys. Rev. A **95**, 062321 (2017).

[15] Y. Wu and X. Yang, Strong-Coupling Theory of Periodically Driven Two-Level Systems, Phys. Rev. Lett. **98**, 013601 (2007).

[16] L. B. Nguyen, Y.-H. Lin, A. Somoroff, R. Mencia, N. Grabon, and V. E. Manucharyan, High-Coherence Fluxonium Qubit, Phys. Rev. X **9**, 041041 (2019).

[17] A. Somoroff, Q. Ficheux, R. A. Mencia, H. Xiong, R. V. Kuzmin, and V. E. Manucharyan, Millisecond coherence in a superconducting qubit (2021), ArXiv:2103.08578.

[18] F. Bao, *et al.*, Fluxonium: An Alternative Qubit Platform for High-Fidelity Operations, Phys. Rev. Lett. **129**, 010502 (2022).

[19] I. N. Moskalenko, I. A. Simakov, N. N. Abramov, A. A. Grigorev, D. O. Moskalev, A. A. Pishchimova, N. S. Smirnov, E. V. Zikiy, I. A. Rodionov, and I. S. Besedin, High fidelity two-qubit gates on fluxoniums using a tunable coupler (2022), ArXiv:2203.16302.

[20] Q. Ficheux, L. B. Nguyen, A. Somoroff, H. Xiong, K. N. Nesterov, M. G. Vavilov, and V. E. Manucharyan, Fast Logic with Slow Qubits: Microwave-Activated Controlled-*Z* Gate on Low-Frequency Fluxoniums, Phys. Rev. X **11**, 021026 (2021).

[21] H. Xiong, Q. Ficheux, A. Somoroff, L. B. Nguyen, E. Dogan, D. Rosenstock, C. Wang, K. N. Nesterov, M. G. Vavilov, and V. E. Manucharyan, Arbitrary controlled-phase gate on fluxonium qubits using differential ac-Stark shifts (2021), ArXiv:2103.04491.

[22] Y. Chen, K. N. Nesterov, V. E. Manucharyan, and M. G. Vavilov, Fast Flux Entangling Gate for Fluxonium Circuits, Phys. Rev. Appl. **18**, 034027 (2022).

[23] K. N. Nesterov, Q. Ficheux, V. E. Manucharyan, and M. G. Vavilov, Proposal for Entangling Gates on Fluxonium

Qubits via a Two-Photon Transition, PRX Quantum **2**, 020345 (2021).

[24] I. N. Moskalenko, I. S. Besedin, I. A. Simakov, and A. V. Ustinov, Tunable coupling scheme for implementing two-qubit gates on fluxonium qubits, Appl. Phys. Lett. **119**, 194001 (2021).

[25] K. N. Nesterov, C. Wang, V. E. Manucharyan, and M. G. Vavilov, CNOT Gates for Fluxonium Qubits via Selective Darkening of Transitions, Phys. Rev. Appl. **18**, 034063 (2022).

[26] T. Q. Cai, J. H. Wang, Z. L. Wang, X. Y. Han, Y. K. Wu, Y. P. Song, and L. M. Duan, All-microwave nonadiabatic multiqubit geometric phase gate for superconducting qubits, Phys. Rev. Res. **3**, 043071 (2021).

[27] K. N. Nesterov, I. V. Pechenezhskiy, C. Wang, V. E. Manucharyan, and M. G. Vavilov, Microwave-activated controlled-*Z* gate for fixed-frequency fluxonium qubits, Phys. Rev. A **98**, 030301(R) (2018).

[28] L. B. Nguyen, G. Koolstra, Y. Kim, A. Morvan, T. Chistolini, S. Singh, K. N. Nesterov, C. Jünger, L. Chen, Z. Pedramrazi, B. K. Mitchell, J. M. Kreikebaum, S. Puri, D. I. Santiago, and I. Siddiqi, Blueprint for a High-Performance Fluxonium Quantum Processor, PRX Quantum **3**, 037001 (2022).

[29] M. Grajcar, Y.-x. Liu, F. Nori, and A. M. Zagoskin, Switchable resonant coupling of flux qubits, Phys. Rev. B **74**, 172505 (2006).

[30] A. M. van den Brink, A. J. Berkley, and M. Yalowsky, Mediated tunable coupling of flux qubits, New J. Phys. **7**, 230 (2005).

[31] A. O. Niskanen, Y. Nakamura, and J.-S. Tsai, Tunable coupling scheme for flux qubits at the optimal point, Phys. Rev. B **73**, 094506 (2006).

[32] S. H. W. van der Ploeg, A. Izmalkov, A. M. van den Brink, U. Hübner, M. Grajcar, E. Il'ichev, H.-G. Meyer, and A. M. Zagoskin, Controllable Coupling of Superconducting Flux Qubits, Phys. Rev. Lett. **98**, 057004 (2007).

[33] A. O. Niskanen, K. Harrabi, F. Yoshihara, Y. Nakamura, S. Lloyd, and J. S. Tsai, Quantum coherent tunable coupling of superconducting qubits, Science **316**, 723 (2007).

[34] M. R. Geller, E. Donate, Y. Chen, M. T. Fang, N. Leung, C. Neill, P. Roushan, and J. M. Martinis, Tunable coupler for superconducting xmon qubits: Perturbative nonlinear model, Phys. Rev. A **92**, 012320 (2015).

[35] Y. Chen, C. Neill, P. Roushan, N. Leung, M. Fang, R. Barends, J. Kelly, B. Campbell, Z. Chen, B. Chiaro, A. Dunsworth, E. Jeffrey, A. Megrant, J. Y. Mutus, P. J. J. O'Malley, C. M. Quintana, D. Sank, A. Vainsencher, J. Wenner, T. C. White, M. R. Geller, A. N. Cleland, and J. M. Martinis, Qubit Architecture with High Coherence and Fast Tunable Coupling, Phys. Rev. Lett. **113**, 220502 (2014).

[36] D. C. McKay, C. J. Wood, S. Sheldon, J. M. Chow, and J. M. Gambetta, Efficient *Z* gates for quantum computing, Phys. Rev. A **96**, 022330 (2017).

[37] J. Chen, D. Ding, C. Huang, and Q. Ye, Compiling arbitrary single-qubit gates via the phase-shifts of microwave pulses (2021), ArXiv:2105.02398.

[38] E. Lucero, J. Kelly, R. C. Bialczak, M. Lenander, M. Mariantoni, M. Neeley, A. D. O'Connell, D. Sank, H. Wang, M. Weides, J. Wenner, T. Yamamoto, A. N. Cleland, and J. M. Martinis, Reduced phase error through optimized control of a superconducting qubit, Phys. Rev. A **82**, 042339 (2010).

[39] J. Koch, V. E. Manucharyan, M. H. Devoret, and L. I. Glazman, Charging Effects in the Inductively Shunted Josephson Junction, Phys. Rev. Lett. **103**, 217004 (2009).

[40] V. E. Manucharyan, J. Koch, L. I. Glazman, and M. H. Devoret, Fluxonium: Single Cooper-pair circuit free of charge offsets, Science **326**, 113 (2009).

[41] M. Peruzzo, A. Trioni, F. Hassani, M. Zemlicka, and J. M. Fink, Surpassing the Resistance Quantum with a Geometric Superinductor, Phys. Rev. Appl. **14**, 044055 (2020).

[42] M. Peruzzo, F. Hassani, G. Szep, A. Trioni, E. Redchenko, M. Žemlička, and J. M. Fink, Geometric Superinductance Qubits: Controlling Phase Delocalization across a Single Josephson Junction, PRX Quantum **2**, 040341 (2021).

[43] D. Gusenkova, M. Spiecker, R. Gebauer, M. Willsch, D. Willsch, F. Valenti, N. Karcher, L. Grünhaupt, I. Takmakov, P. Winkel, D. Rieger, A. V. Ustinov, N. Roch, W. Wernsdorfer, K. Michielsen, O. Sander, and I. M. Pop, Quantum Nondemolition Dispersive Readout of a Superconducting Artificial Atom Using Large Photon Numbers, Phys. Rev. Appl. **15**, 064030 (2021).

[44] I. M. Pop, K. Geerlings, G. Catelani, R. J. Schoelkopf, L. I. Glazman, and M. H. Devoret, Coherent suppression of electromagnetic dissipation due to superconducting quasiparticles, Nature **508**, 369 (2014).

[45] A. Kou, W. C. Smith, U. Vool, R. T. Brierley, H. Meier, L. Frunzio, S. M. Girvin, L. I. Glazman, and M. H. Devoret, Fluxonium-Based Artificial Molecule with a Tunable Magnetic Moment, Phys. Rev. X **7**, 031037 (2017).

[46] J. R. Schrieffer and P. A. Wolff, Relation between the Anderson and Kondo Hamiltonians, Phys. Rev. **149**, 491 (1966).

[47] C. Cohen-Tannoudji, J. Dupont-Roc, and G. Grynberg, *Atom-Photon Interactions* (John Wiley & Sons, Ltd, 1998) Chap. 1, p. 38.

[48] R. Winkler, *Spin-Orbit Coupling Effects in Two-Dimensional Electron and Hole Systems* (Springer, Berlin, 2003), 201

[49] G. Zhu, D. G. Ferguson, V. E. Manucharyan, and J. Koch, Circuit QED with fluxonium qubits: Theory of the dispersive regime, Phys. Rev. B **87**, 024510 (2013).

[50] G. Zhu and J. Koch, Asymptotic expressions for charge-matrix elements of the fluxonium circuit, Phys. Rev. B **87**, 144518 (2013).

[51] P. Mundada, G. Zhang, T. Hazard, and A. Houck, Suppression of Qubit Crosstalk in a Tunable Coupling Superconducting Circuit, Phys. Rev. Appl. **12**, 054023 (2019).

[52] M. D. Hutchings, J. B. Hertzberg, Y. Liu, N. T. Bronn, G. A. Keefe, M. Brink, J. M. Chow, and B. L. T. Plourde, Tunable Superconducting Qubits with Flux-Independent Coherence, Phys. Rev. Appl. **8**, 044003 (2017).

[53] P. Krantz, M. Kjaergaard, F. Yan, T. P. Orlando, S. Gustavsson, and W. D. Oliver, A quantum engineer's guide to superconducting qubits, Appl. Phys. Rev. **6**, 021318 (2019).

[54] S. Poletto, F. Chiarello, M. G. Castellano, J. Lisenfeld, A. Lukashenko, C. Cosmelli, G. Torrioli, P. Carelli, and A. V. Ustinov, Coherent oscillations in a superconducting tunable flux qubit manipulated without microwaves, New J. Phys. **11**, 013009 (2009).

[55] Many other simple pulse shapes, such as those utilized in Ref. [8], achieve net-zero flux and can yield high-fidelity gates. Single-period sinusoids are used here for simplicity.

[56] M. A. Rol, F. Battistel, F. K. Malinowski, C. C. Bultink, B. M. Tarasinski, R. Vollmer, N. Haider, N. Muthusubramanian, A. Bruno, B. M. Terhal, and L. DiCarlo, Fast, High-Fidelity Conditional-Phase Gate Exploiting Leakage Interference in Weakly Anharmonic Superconducting Qubits, Phys. Rev. Lett. **123**, 120502 (2019).

[57] Z. Huang, P. S. Mundada, A. Gyenis, D. I. Schuster, A. A. Houck, and J. Koch, Engineering Dynamical Sweet Spots to Protect Qubits from $1/f$ Noise, Phys. Rev. Appl. **15**, 034065 (2021).

[58] L. H. Pedersen, N. M. Møller, and K. Mølmer, Fidelity of quantum operations, Phys. Lett. A **367**, 47 (2007).

[59] P. Groszkowski and J. Koch, SCQUBITS: a PYTHON package for superconducting qubits, Quantum **5**, 583 (2021).

[60] J. R. Johansson, P. D. Nation, and F. Nori, QuTiP: An open-source PYTHON framework for the dynamics of open quantum systems, Comput. Phys. Commun. **183**, 1760 (2012).

[61] J. R. Johansson, P. D. Nation, and F. Nori, QuTiP 2: A PYTHON framework for the dynamics of open quantum systems, Comput. Phys. Commun. **184**, 1234 (2013).

[62] J. H. Shirley, Solution of the Schrodinger Equation with a Hamiltonian Periodic in Time, Phys. Rev. **252**, 424 (1965).

[63] A. Petrescu, C. L. Calonnec, C. Leroux, A. Di Paolo, P. Mundada, S. Sussman, A. Vrajitoarea, A. A. Houck, and A. Blais, Accurate methods for the analysis of strong-drive effects in parametric gates (2021), ArXiv:2107.02343.

[64] The reason why we keep the treatment general enough to include multiple drive periods will become clear when we consider time evolution on the full system: for realistic parameters, a single drive period leads to drive amplitudes that are so large that we obtain fidelity-degrading contributions from high-lying coupler states.

[65] A gate with $|a| = |d| = 1/\sqrt{2}$ and $|c| = 0$ is also entangling, yielding a $\sqrt{b\text{SWAP}}$-like gate [84]. Here, we focus instead on entangling gates performed in the $|\overline{01}\rangle, |\overline{10}\rangle$ subspace rather than in the $|\overline{00}\rangle, |\overline{11}\rangle$ subspace.

[66] V. Vedral, M. B. Plenio, M. A. Rippin, and P. L. Knight, Quantifying Entanglement, Phys. Rev. Lett. **78**, 2275 (1997).

[67] C. Huang, T. Wang, F. Wu, D. Ding, Q. Ye, L. Kong, F. Zhang, X. Ni, Z. Song, Y. Shi, H.-H. Zhao, C. Deng, and J. Chen, Quantum instruction set design for performance (2021), ArXiv:2105.06074.

[68] X. Mi, P. Roushan, C. Quintana, S. Mandrà, J. Marshall, C. Neill, F. Arute, K. Arya, J. Atalaya, and R. Babbush, *et al.*, Information scrambling in quantum circuits, Science **374**, 1479 (2021).

[69] F. Arute, K. Arya, R. Babbush, D. Bacon, J. C. Bardin, R. Barends, S. Boixo, M. Broughton, B. B. Buckley, and D. A. Buell, *et al.*, Hartree-Fock on a superconducting qubit quantum computer, Science **369**, 1084 (2020).

[70] F. Bloch and A. Siegert, Magnetic resonance for nonrotating fields, Phys. Rev. **57**, 522 (1940).

[71] The off position is found by minimizing the energy of the $|\overline{11}\rangle$ state, analogously to how the off position is found based on the effective Hamiltonian H_{eff}. The exact and effective values for the coupler flux at the off position typically have a relative deviation of less than one percent.

[72] M. A. Nielsen and I. L. Chuang, *Quantum Computation and Quantum Information: 10th Anniversary Edition* (Cambridge University Press, 2010) Chap. 8.

[73] J. M. Chow, J. M. Gambetta, L. Tornberg, J. Koch, L. S. Bishop, A. A. Houck, B. R. Johnson, L. Frunzio, S. M. Girvin, and R. J. Schoelkopf, Randomized Benchmarking and Process Tomography for Gate Errors in a Solid-State Qubit, Phys. Rev. Lett. **102**, 090502 (2009).

[74] M. A. Nielsen, A simple formula for the average gate fidelity of a quantum dynamical operation, Phys. Lett. A **303**, 249 (2002).

[75] M. Horodecki, P. Horodecki, and R. Horodecki, General teleportation channel, singlet fraction, and quasidistillation, Phys. Rev. A **60**, 1888 (1999).

[76] We are following the current common practice of utilizing the Lindblad master equation to obtain open-system gate-fidelity estimates. It remains an open question whether this standard treatment is sufficient to accurately predict fidelities with an increasing number of "9"s.

[77] A. G. Fowler, M. Mariantoni, J. M. Martinis, and A. N. Cleland, Surface codes: Towards practical large-scale quantum computation, Phys. Rev. A **86**, 032324 (2012).

[78] J. D. Hunter, MATPLOTLIB: A 2D graphics environment, Comput. Sci. Eng. **9**, 90 (2007).

[79] C. R. Harris, K. J. Millman, S. J. van der Walt, R. Gommers, P. Virtanen, D. Cournapeau, E. Wieser, J. Taylor, S. Berg, and N. J. Smith, *et al.*, Array programming with NumPy, Nature **585**, 357 (2020).

[80] P. Virtanen, R. Gommers, T. E. Oliphant, M. Haberland, T. Reddy, D. Cournapeau, E. Burovski, P. Peterson, W. Weckesser, and J. Bright, *et al.*, SciPy 1.0: Fundamental Algorithms for Scientific Computing in PYTHON, Nat. Methods **17**, 261 (2020).

[81] U. Vool and M. Devoret, Introduction to quantum electromagnetic circuits, Int. J. Circuit Theory Appl. **45**, 897 (2017).

[82] X. You, J. A. Sauls, and J. Koch, Circuit quantization in the presence of time-dependent external flux, Phys. Rev. B **99**, 174512 (2019).

[83] J. J. Sakurai and J. Napolitano, *Modern Quantum Mechanics*, 2nd ed. (Cambridge University Press, 2017) Chap. 5, p. 358.

[84] S. Poletto, J. M. Gambetta, S. T. Merkel, J. A. Smolin, J. M. Chow, A. D. Córcoles, G. A. Keefe, M. B. Rothwell, J. R. Rozen, D. W. Abraham, C. Rigetti, and M. Steffen, Entanglement of Two Superconducting Qubits in a Waveguide Cavity via Monochromatic Two-Photon Excitation, Phys. Rev. Lett. **109**, 240505 (2012).